



Layered $\text{Na}_2\text{Mn}_3\text{O}_7$ decorated by Cerium as the robust catalysts for efficient low temperature soot combustion

Di Yu^{a,b}, Xuehua Yu^{a,*}, Chunlei Zhang^a, Lanyi Wang^b, Xiaoqiang Fan^a, Zhen Zhao^{a,b,**}, Yuechang Wei^b, Jian Liu^b, Joanna Gryboś^c, Bartosz Leszczyński^d, Anna Wach^e, Dominik Wierzbicki^e, Andrzej Kotarba^c, Zbigniew Sojka^{c,*}

^a Institute of Catalysis for Energy and Environment, College of Chemistry and Chemical Engineering, Shenyang Normal University, Shenyang 110034, China

^b State Key Laboratory of Heavy Oil Processing, China University of Petroleum, Beijing 102249, China

^c Faculty of Chemistry, Jagiellonian University, ul. Gronostajowa 2, 30-387 Krakow, Poland

^d M. Smoluchowski Institute of Physics, Jagiellonian University, ul. Łojasiewicza 11, 30-387 Krakow, Poland

^e Paul Scherrer Institute, Forschungsstrasse 111, 5232 Villigen PSI, Switzerland

ARTICLE INFO

Keywords:

Layered manganese oxides
Cerium
Low temperature
Soot combustion
Catalysts

ABSTRACT

Removal of soot particles by highly efficient catalysts is a research hotspot, not only because the problem of air pollution, but also because the complexity of the catalytic process that involves gas-solid-solid three-phase reaction. We synthesized single atom Ce and CeO_2 nanoparticles simultaneously modified layered $\text{Na}_2\text{Mn}_3\text{O}_7$ catalysts for soot combustion with unprecedented catalytic performance and high resistance to water and sulfur, using low-cost raw materials and a simple preparation protocol. The synergy between the easily available adsorbed and surface reactive oxygen species and the high yield of NO_2 exploitation, leads to the beneficial transition of soot combustion process from “gas-solid-solid” into “gas-gas-solid”, thereby, shifted to low temperatures. Our findings provide a pathway to the development of cheap catalysts based on transition metal oxides, avoiding application of noble metals for successful elimination of diesel exhausts at remarkably low temperatures.

1. Introduction

Soot particles ($\text{PM}_{2.5}$) released from diesel engines have been considered as a main source of urban atmospheric pollution, which is directly threatening the environment and peoples' health [1,2]. Catalytic removal of soot particles during the after-treatment of diesel exhausts is one of the most perspective environmental technologies [3,4]. Thus, development of robust catalysts is a key factor for efficient soot combustion. Due to the three-phase character of the gas(O_2)-solid (soot)-solid(catalyst) interactions for soot combustion, it is extremely important to improve the contact efficiency between the catalyst and soot particles [5,6]. Meantime, as a thermal catalytic oxidation reaction, soot combustion is also deeply affected by the intrinsic activity of the catalysts [7–9]. Therefore, design and preparation of novel catalysts with high inherent activity and contact efficiency are important for making a substantial progress in soot combustion catalysis. Nowadays,

various kinds of catalytic systems have been explored and applied for soot combustion. To enhance the contact efficiency, the novel catalysts with different morphologies have been designed, such as space-open arrays, three-dimensionally networked, fibrous and three-dimensionally ordered macroporous (3DOM) structures, and found to exhibit good catalytic performance [10–15]. For the improvement of intrinsic activity, supported noble metal catalysts (e.g., Au, Pt, Ag and Pd) have been widely studied for soot combustion owing to their excellent low temperature performance and superior oxidation-reduction quality [16–22]. However, owing to high cost and natural scarcity, a wider application of the noble metal catalysts is limited. Thus, development of novel and non-noble metal containing catalytic materials with good intrinsic activity and decent contact efficiency has recently become a research hotspot.

Manganese oxides, as one kind of abundant transition metal oxides, which have the advantages of low-cost, environment-friendliness,

* Corresponding authors.

** Corresponding author at: Institute of Catalysis for Energy and Environment, College of Chemistry and Chemical Engineering, Shenyang Normal University, Shenyang 110034, China.

E-mail addresses: yuxuehua1986@163.com (X. Yu), zhenzhao@cup.edu.cn, zhaozhen1586@163.com (Z. Zhao), sojka@chemia.uj.edu.pl (Z. Sojka).

<https://doi.org/10.1016/j.apcatb.2023.123022>

Received 16 April 2023; Received in revised form 17 June 2023; Accepted 19 June 2023

Available online 20 June 2023

0926-3373/© 2023 Elsevier B.V. All rights reserved.

unique redox properties associated with the easily achievable variable valence states (Mn^{2+} , Mn^{3+} and Mn^{4+}). They have widely been applied in various fields, such as catalysis, electronics, sorption and gas sensor devices [23–28]. For soot combustion, manganese oxides with crystal structures of octahedral molecular sieves (OMS-2) and octahedral layered structure (OL-1) show better catalytic activity than other crystal structures. Potassium is functioning not only as a structure stabilizer and low melting point agent, but also exhibits a pronounced electron donation capacity. Hence, potassium ions were usually doped into the above crystal structures to form K-OMS-2 and K-OL-1 materials, thereby improving catalytic activity [29–31]. As another alkali metal, sodium may be expected to share similar advantages of potassium for soot combustion [32]. Therefore, Na doped manganese oxides can be regarded as promising high-efficiency catalysts for this purpose. Delmas et al. have performed pioneering studies on the family of Na_xMnO_2 oxides, especially on the 2D-type structures obtained for $x = 0.6, 0.7$ and 1 [33]. The layered Na-Mn-O system completely fulfills the requirements in terms of low price, low toxicity and excellent catalytic performance for various oxidation reactions [34–36]. At present, among the Na-Mn-O materials, $\text{Na}_2\text{Mn}_3\text{O}_7$ with the layer structure has been widely studied for prospective applications as an electrode material for Na-ion batteries, due to its high energy density and efficiency by exploiting the lattice anionic redox [37–39]. However, as a catalyst for soot combustion, the performance of $\text{Na}_2\text{Mn}_3\text{O}_7$ has not been significantly explored so far. In addition, CeO_2 exhibits high oxygen storage/release capacity because of the unique reversible $\text{Ce}^{4+}/\text{Ce}^{3+}$ redox, which can provide oxygen in a reducing atmosphere and store oxygen in an oxidation atmosphere [40–42]. Therefore, cerium has been extensively applied in three-way catalysts for elimination of gasoline vehicle exhausts [43,44]. For soot combustion, CeO_2 -based oxides have been examined as promising catalysts [45,46], and catalysts component [47, 48], as well. However, design and preparation of novel catalysts, which can effectively combine low-cost Na, Mn and Ce elements into a catalytically functional system of beneficial structure and morphology, is still a challenge.

Herein, we designed and explored new type of single atom Ce and CeO_2 nanoparticles (NPs) co-modified layered-type $\text{Na}_2\text{Mn}_3\text{O}_7$ catalysts ($\text{Ce-Na}_2\text{Mn}_3\text{O}_7$). The structure of the catalyst characterized by a simple formulation that only require low cost raw materials and straightforward synthesis protocol, which exhibit excellent activity, stability and resistance to water and sulfur in soot combustion. The synergistic effect of the composition and morphology of the $\text{Ce-Na}_2\text{Mn}_3\text{O}_7$ catalytic materials has been identified for the first time. Moreover, high-efficiency of $\text{Ce-Na}_2\text{Mn}_3\text{O}_7$ catalysts for soot combustion was achieved at spectacularly low temperatures ($T_{90} < 400^\circ\text{C}$) under the loose soot-catalyst contact condition, even in the presence of all contaminants (SO_2 and H_2O).

2. Experimental section

2.1. Catalysts preparation

2.1.1. Chemicals and materials

Manganese nitrate ($\text{Mn}(\text{NO}_3)_2$, 50% aqueous solution), Sodium nitrate (NaNO_3 , AR), Cerium(III) nitrate hexahydrate ($\text{Ce}(\text{NO}_3)_3 \cdot 6\text{H}_2\text{O}$, AR), D(+)-Glucose monohydrate ($\text{C}_6\text{H}_{12}\text{O}_6 \cdot \text{H}_2\text{O}$) were purchased from Sinopharm Group Chemical Reagent Co. Ltd. All chemicals are of analytical grades and were used without further purification.

2.1.2. Synthesis of $n\%\text{Ce-Na}_2\text{Mn}_3\text{O}_7$ catalysts

In a typical process, 3.58 g of $\text{Mn}(\text{NO}_3)_2$ (50% aqueous solution), 0.42 g of NaNO_3 and a certain amount of $\text{Ce}(\text{NO}_3)_3 \cdot 6\text{H}_2\text{O}$ were dissolved in 20 mL deionized water to form a clarified solution. Afterwards, 3.96 g of glucose was added into the above solution and the mixture stirred for 2 h at room temperature. The precursor products were dried at 80°C for 48 h, and then calcined at thermal treatment temperature of

550°C for 4 h at a rate of $5^\circ\text{C}/\text{min}$. The as-prepared samples were denoted by $n\%\text{Ce-Na}_2\text{Mn}_3\text{O}_7$, where $n\%$ is the molar ratios for Ce/Mn of 0, 0.05%, 0.1%, 0.5%, 1%, 5, 10%, 20%, and 50%, respectively.

2.1.3. Synthesis of CeO_2 , MnO_x , $1\%\text{Ce-MnO}_x$ and $50\%\text{Na-CeO}_2$ catalysts

According to the raw material composition with given stoichiometry, CeO_2 , MnO_x , $1\%\text{Ce-MnO}_x$ and $50\%\text{Na-CeO}_2$ catalysts were prepared by the same synthesis steps as described above. The synthetic recipes for the preparation of as-prepared catalysts are described in the Table S1.

2.2. Physical and chemical characterization

XRD patterns were performed on a powder X-ray diffractometer (Ultima IV, Rigaku) using Cu K α radiation as the source with a Ni filter. Data were collected from 10° to 80° (2θ) at a scanning speed of $5^\circ/\text{min}$. Raman spectra were recorded on a HORIBA LabRAM HR evolution spectrometer with a 325 nm laser. X-ray photoelectron spectroscopy characterization (XPS) was conducted on a Thermo ESCALAB 250Xi instrument. The binding energy was calibrated with C1s located at 284.8 eV.

SEM images were acquired with a field emission scanning electron microscopy (Quanta 200 F, FEI). TEM and HRTEM images were carried on using a JEM 2100 LaB $_6$ transmission electron microscope (JEOL). HAADF-STEM imaging and elemental mapping was performed using a Talos F200 (Thermo Fisher Scientific) and a Tecnai-Osiris transmission electron microscopes operating at 200 kV. The aberration-corrected HAADF-STEM images were obtained on JEOL JEM-ARM300F and Titan (FEI) microscope at 300 kV. The catalyst samples were placed on the copper grid covered with a holey carbon film. The EDX analysis was carried out with a windowless 4-sector silicon drift detector (Super-X EDX) and the Bruker ESPRIT software. Prior to microscopic observations, the samples dispersed in ethanol were placed on the copper grid covered with a holey carbon film.

X-band EPR spectra were recorded at room and liquid nitrogen temperatures using a Bruker ELEXYS 580 spectrometer and a TE102 cavity with 100 kHz modulation.

Computed X-ray microtomographic (μ -CT) imaging of the samples was performed using a Bruker SkyScan 1172 micro-CT scanner with the energy of 80 keV. The 2000×1332 pixel projection images with the size of $1.38\ \mu\text{m}$ were recorded with the rotation steps of 0.4° . The reconstructed image stacks were median filtered with a 3 pixel circular kernel, and for distinction of the boundaries a histogram-based threshold was applied.

XAS measurement were performed at SuperXAS – X10DA beamline of the SLS at Paul Scherrer Institute in Villigen, Switzerland. Measurements were performed with a focus beam diameter $\sim 100\ \mu\text{m}$, with Si (111) monochromator. For the measurements Ce L3 (5723 eV) and Mn K- (6539 eV) edges were selected. For the XAS and XES signal detection Vortex and Von Hamos detectors were used. As the reference the following samples were measured: MnO , Mn_3O_4 , Mn_2O_3 , MnO_2 , CeO_2 , $\text{Ce}(\text{NO}_3)_3$. For the measurements quartz capillaries with the following parameters: length 80 mm, diameter 1.5 mm, wall thickness 0.01 mm were used. For in situ experiments $5\%\text{O}_2/\text{He}$, $1\%\text{NO}$ in Argon and $5\%\text{O}_2/\text{He}-1\%\text{NO}$ in Argon mixture were used with the total gas flow of $\sim 30\ \text{mL}/\text{min}$. In situ experiment were carried out up to 700°C and the reaction products were detected by a mass spectrometer. Furthermore, Ce L-edge analysis was performed with Si (111) crystal monochromators at the BL11B beamlines at the Shanghai Synchrotron Radiation Facility (SSRF) (Shanghai, China). Before the analysis at the beamline, samples were pressed into thin sheets with 1 cm in diameter and sealed using Kapton tape film. The XAFS spectra were recorded at room temperature using a 4-channel Silicon Drift Detector (SDD) Bruker 5040. Ce L-edge extended X-ray absorption fine structure (EXAFS) spectra were recorded in transmission mode. The XAFS spectra of CeO_2 standard sample were recorded in transmission mode. EXAFS fitting were performed and analyzed with the Athena and Artemis programs of the Demeter data

analysis packages [49] that utilizes the FEFF6 program [50] to fit the EXAFS data. The energy calibration of the sample was conducted through a standard V foil, which as a reference was simultaneously measured. A linear function was subtracted from the pre-edge region, then the edge jump was normalized using Athena software. The $\chi(k)$ data were isolated by subtracting a smooth, third-order polynomial approximating the absorption background of an isolated atom. The k^2 -weighted $\chi(k)$ data were Fourier transformed after applying a Hanning window function ($\Delta k = 2.0$). For Wavelet Transform analysis, the $\chi(k)$ exported from Athena was imported into the Hama Fortran code [51]. The parameters were listed as follow: R -range, 1–3.5 Å, k -range, 0–13.0 Å⁻¹ for sample (0–13.0 Å⁻¹ for CeO₂); k weight, 2; and Morlet function with $\kappa = 9$, $\sigma = 1$ was used as the mother wavelet to provide the overall distribution.

H₂-TPR measurements were operated on a TP-5076 adsorption instrument (Tianjin, China). A sample of 50 mg was placed in a fixed-bed tubular quartz reactor and pre-treated in flowing N₂ at 300 °C for 1 h. After cooling to 50 °C, the gas flow was switched to 50 mL/min 10 vol% H₂/N₂ and the temperature ramped from 50 °C to 800 °C at a rate of 10 °C/min. The consumption of hydrogen in the reduction peaks was calculated by using the H₂-TPR curve of CuO powder [52,53].

O₂-TPD measurements were also carried on the same instrument. At first, a sample of 100 mg was pre-treated in Ar at 300 °C for 1 h followed by cooling to 50 °C, and then the sample was treated at 50 °C under O₂ flow to form the adsorbed oxygen species. Subsequently, the flow gas was switched to 50 mL/min He and the temperature was heated to 800 °C at 10 °C/min after purging for 30 min.

Soot-TPR measurements were performed in 50 mL/min of Ar atmosphere and the gas composition from Soot-TPR is monitored by an Agilent 7890B gas chromatograph. The mixture of 100 mg catalyst and 10 mg soot obtained under loose contact was pretreated in Ar (50 mL/min) at 200 °C for 30 min to remove impurities. Then, the outlet gases were analyzed by the on-line GC under the same atmosphere in the temperature range of 100 °C to 600 °C at 2 °C/min.

NO-TPO measurements were conducted on a NO_x Analyzer (nCLD 62). Before analysis, the catalysts were pre-treated at 200 °C in 50 mL/min of Ar for 30 min followed by cooling to 100 °C, and then the sample was treated at 100 °C under the flow of 10% O₂, 2000 ppm NO and Ar balanced (flow rate 50 mL/min) until the baseline was stable. After that, the pre-treated catalysts were raised from 100 to 500 °C with a temperature ramp of 2 °C/min under the same condition.

In-situ DRIFT spectra were recorded on a Vertex 80 v spectrometer (Bruker). In each experiment, the samples were pre-treated at 300 °C in an Ar atmosphere for 30 min and then reduced to room temperature. Then, the flow was switched to a gas mixture of 10% O₂, 2000 ppm NO and Ar (50 mL/min). The spectra were collected from 800 to 2000 cm⁻¹ with a resolution of 4 cm⁻¹ at the target temperatures. The reference sample of SiO₂ (Quartz sand) was obtained from Tianjin Guangfu Technology Development Co., Ltd.

The concept for degree of relative contact (DRC), which is related to the contact efficiency, was calculated by the following formula:

$$DRC = 1 - \frac{T_{50}(LC) - T_{50}(TC)}{T_{50}(TC)} \approx 1 - \frac{T_{90}(LC) - T_{90}(TC)}{T_{90}(TC)}$$

Where T_{50} and T_{90} represent the temperature of 50% and 90% soot conversion, and LC and TC represent the loose and tight contact mode, respectively [54,75]. The T_{50} and T_{90} values of catalysts under loose and tight contact mode were derived from the TPO reaction and acquired through an Agilent 7890B gas chromatograph. In the typical experiment, 100 mg catalyst and 10 mg soot were mixed by a spatula to a loose contact mode, whereas catalyst and soot with the same mass ratio was placed in an agate mortar and ground for 10 min to obtain a tight contact mode.

Apparent activation energy (E_a) of catalysts for soot combustion reaction were calculated by Arrhenius method. The specific formula based

on the Arrhenius method was as follows:

$$\frac{d[\ln(\frac{\alpha}{T^2})]}{d(\frac{1}{T})} = -\frac{E_a}{R}$$

where α is the reaction heating rate (K/min), T is the temperature corresponding to different soot conversion from 10% to 90%, and R is the gas constant of 8.314 J/(mol·K), E_a is the apparent activation energy (kJ/mol). The T values with the heating rates of 2, 4, 6 and 8 K/min were calculated by detecting the outlet gas composition through an Agilent 7890B gas chromatograph. The E_a for soot combustion reaction was estimated from the slope of the best-fitting line when $\ln(\alpha/T^2)$ was plotted versus $1/T$.

Periodic DFT + U modeling was performed with the VASP code using a projector augmented plane wave method (PAW), the PBE exchange-functional and the Hubbard parameter $U = 2.5$ eV for manganese cations. For bulk calculations the $3 \times 3 \times 5$ sampling mesh of the Monkhorst-Pack grid was used, whereas for slab calculations the $3 \times 3 \times 1$ sampling mesh was applied. The cutoff energy was set to 420 eV. The bulk Na₂Mn₃O₇ unit cell containing 24 ions (Na₂Mn₃O₇), and a (2×2) slab model exposing the (1–10) plane were used. A slab model was composed by 9 at. layers (~16 Å) and the vacuum separation of 15 Å. Only the atoms located in the top layers were relaxed. The convergence value was set to 10^{-4} eV·Å⁻¹.

To examine the defects structure, O₂, NO, NO₂ and NO₃ adsorption on the exposed (1–10) surfaces under various temperature and pressure conditions, the ab-initio thermodynamic modeling was applied. The free energy, γ , of the surface covered by N_x atoms of the gas reactants and N_{Mn} manganese atoms relative to the bulk Na₂Mn₃O₇, taking oxygen as an example, can be calculated as:

$$\gamma(T, p_{O_2}) = \frac{1}{2A} \left[G_{Na_2Mn_3O_7}^{slab}(T, p_{O_2}, N_{mn}, N_O) - N_{mn} G_{Na_2Mn_3O_7}^{bulk} - \left(N_O - \frac{7}{3} N_{mn} \right) \mu_O(T, p_{O_2}) \right]$$

In the above equation, $G_{Na_2Mn_3O_7}^{slab}$ and $G_{Na_2Mn_3O_7}^{bulk}$ correspond to the free energy of the slab and the bulk, respectively, normalized to a formula unit (Na₂Mn₃O₇). The entropic vibrational contributions to the Gibbs free energies cancel to a large extent, thus their values were approximated by the corresponding DFT energies. The symbol A stands for the (1×1) surface area exposed by the (1–10) slab, whereas $\mu_O(T, p_{O_2})$ is the chemical potential of dioxygen, factored into the electronic energy ($\frac{1}{2} E_{O_2}^{tot}$), the temperature ($\mu_{O_2}(T, p_{O_2}^0)$), and the pressure ($kT \ln(\frac{p_{O_2}}{p^0})$)-dependant contributions

$$\mu_O(T, p_{O_2}) = \frac{1}{2} E_{O_2}^{tot} + \mu_{O_2}(T, p_{O_2}^0) + kT \ln\left(\frac{p_{O_2}}{p^0}\right)$$

The electronic energy term, $\frac{1}{2} E_{O_2}^{tot}$, was calculated by DFT, whereas the $\mu_{O_2}(T, p_{O_2}^0)$ term was computed by means of standard statistical thermodynamics.

2.3. Catalytic activity measurements

The catalytic activities of as-prepared catalysts for soot combustion were evaluated by temperature-programmed oxidation (TPO) reaction. The TPO reaction was carried out using an on-line gas chromatograph (GC, Agilent 7890B). The model soot was Printex-U particulates (25-nm diameter, Degussa). In each experiment, 100 mg catalyst and 10 mg soot were mixed by a spatula and the loose contact mixture was placed in the fixed-bed tubular quartz reactor ($\Phi = 8$ mm), and the temperature was heated from 100 to 600 °C by a rate of 2 °C/min under an atmosphere containing 10% O₂ and 2000 ppm NO balanced with Ar (50 mL/min). The catalytic activity was evaluated using the values of T_{10} , T_{50} and T_{90} , which were defined as the temperatures for 10%, 50%, and 90% of soot

conversions, respectively. The selectivity to CO_2 (S_{CO_2}) was defined as that the CO_2 outlet concentration (C_{CO_2}) divided by the sum of the CO_2 and CO outlet concentrations, as shown in the following expression:

$$S_{\text{CO}_2} = \frac{C_{\text{CO}_2}}{C_{\text{CO}} + C_{\text{CO}_2}}$$

$S_{\text{CO}_2}^m$ was denoted as S_{CO_2} at the temperature (T_m) corresponding to the highest soot-burnt rate.

In order to investigate the water resistance of catalysts, the as-prepared catalysts were evaluated under the reaction condition of 10% O_2 , 2000 ppm NO and 10% H_2O balanced with Ar at a flow rate 50 mL/min. To explore the sulfur resistance, the activity of catalysts under the mixed gas of 10% O_2 , 2000 ppm NO and 300 ppm SO_2 balanced with Ar was also tested. In addition, the sulfur and water resistance of catalysts was measured under an atmosphere containing 10% H_2O and 100 or 300 ppm SO_2 balanced with Ar. More than that, the catalytic performance with 5-cycles reaction under different conditions were also measured to investigate the stability of as-prepared catalysts.

3. Results and discussion

3.1. Texture properties of $\text{Ce-Na}_2\text{Mn}_3\text{O}_7$ catalysts

The structural and textural properties of the catalysts belong to one of the most crucial factors determining their catalytic performance. The $\text{Ce-Na}_2\text{Mn}_3\text{O}_7$ catalysts were then characterized by XRD, Raman, SEM, TEM, HAADF-STEM and EXAFS techniques. The diffraction peaks located at 2θ of 15.8° , 32.2° and 37.4° , corresponding to the (100), (200) and (102) crystal faces, respectively (Fig. 1 A), are characteristic for $\text{Na}_2\text{Mn}_3\text{O}_7$ of the layered structure (JCPDS Card No. 78-0193). With the increasing Ce-doping, some new diffraction peaks located at 28.5° , 33.0° , 47.4° and 56.3° appear, and grow in the intensity when the mole ratio of Ce:Mn is higher than 5%. Those peaks are related to the (111), (200), (220) and (311) crystal planes of CeO_2 , respectively (JCPDS Card No. 89-8436). This phenomenon indicates that the excess Ce ions may be released from the crystal structure and form well faceted CeO_2 nanoparticles on the surface of $\text{Na}_2\text{Mn}_3\text{O}_7$. The XRD patterns in Fig. S1 show that 1%Ce- MnO_x and MnO_x catalysts display the crystal structure of Mn_2O_3 phase (JCPDS Card No. 71-0636), and the diffraction peaks of 50%Na- CeO_2 and CeO_2 catalysts can be assigned to CeO_2 phase, further exploring the synthesis conditions for the formation of layered

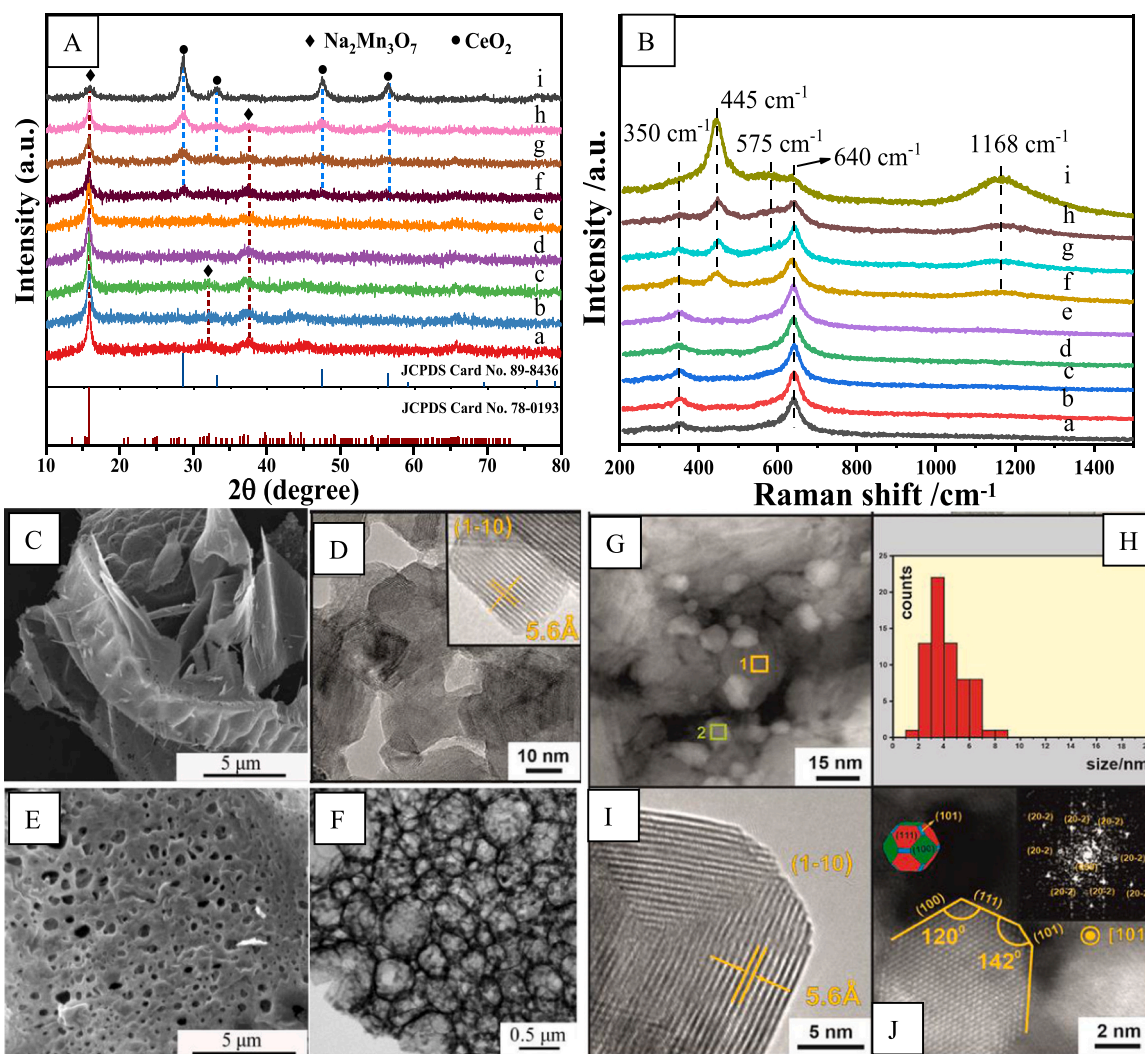


Fig. 1. Left panel shows XRD patterns (A) and Raman spectra (B) of the investigated catalysts (a: bare $\text{Na}_2\text{Mn}_3\text{O}_7$; b: 0.05%; c: 0.1%; d: 0.5%; e: 1%; f: 5%; g: 10%; h: 20%; i: 50% $\text{Ce-Na}_2\text{Mn}_3\text{O}_7$). SEM images of $\text{Na}_2\text{Mn}_3\text{O}_7$ (C) and 1% $\text{Ce-Na}_2\text{Mn}_3\text{O}_7$ (E), TEM and HRTEM images of $\text{Na}_2\text{Mn}_3\text{O}_7$ (D) and 1% $\text{Ce-Na}_2\text{Mn}_3\text{O}_7$ (F and I), HAADF-TEM of images of 1% $\text{Ce-Na}_2\text{Mn}_3\text{O}_7$ (G), particle size distribution of CeO_2 (H), and AC-STEM image of CeO_2 particles in 1% $\text{Ce-Na}_2\text{Mn}_3\text{O}_7$, together with FT diffraction and Wulff shape reconstruction (J). The EDX patterns of the selected regions 1 and 2 are shown in Fig. S5.

manganese oxides and the synergistic effect of Na, Mn, and Ce elements. To probe the local structure of the Ce-Na₂Mn₃O₇ catalysts, Raman spectra were recorded with a 325 nm laser in the range of 200–1500 cm⁻¹. Five Raman peaks located at 350, 454, 575, 640 and 1168 cm⁻¹ can be observed (Fig. 1B). With the increase of Ce-doping, intensity of the peaks at 350 and 640 cm⁻¹ gradually decreases, while those located at 454, 575 and 1168 cm⁻¹ increases. It can be thus inferred that the two peaks at 350 and 640 cm⁻¹ can be associated with Na₂Mn₃O₇, whereas the remaining three peaks (located at 454, 575 and 1168 cm⁻¹) are related to CeO₂. Based on the previous reports, the peak at 640 cm⁻¹ can be assigned to the Mn-O vibrations, along the direction of the MnO₆ octahedral double chains, and the peak at 350 cm⁻¹ can be associated with an asymmetric stretch of the bridge oxygen species (Mn–O–Mn) [55,56]. The peaks at 455, 575 and 1168 cm⁻¹ could be attributed to the F_{2g} vibration mode in the fluorite structure of CeO₂, whereas a defect-induced (D) mode corresponds to an oxygen vacancy, and a second-order longitudinal optical (2LO) mode, respectively [57–59].

Due to the gas(O₂)-solid(soot)-solid(catalyst) type of the heterogeneous catalysis for soot combustion, the morphology of catalysts can enhance the contact efficiency between the soot, and catalyst's particles is of vital importance for improving the activity. The parent Na₂Mn₃O₇ catalysts have the morphology of extended nanosheets, as revealed by SEM and TEM imaging (Fig. 1 C, D and Fig. S2). Compared with Na₂Mn₃O₇, the morphology of the 1% Ce-Na₂Mn₃O₇ catalyst is dramatically changed into distinctly thicker sheets, forming abundant pores with the diameter of about 0.1–0.5 μm (Fig. 1E). All the Ce-Na₂Mn₃O₇ catalysts with different Ce doping levels exhibit also a developed pore structure, with the diameter of pores increasing roughly with the Ce loading (Fig. S2A–G). The morphologies of the reference 50%Na-CeO₂, 1%Ce-MnO_x, MnO_x and CeO₂ samples are shown in Fig. S2H–K, as well. Compared with the Ce-Na₂Mn₃O₇ catalysts, the 1% Ce-MnO_x and MnO_x reference materials assume also the shape of nanosheets, while the 50%Na-CeO₂ and CeO₂ have foam-like morphologies. The abundant pores in the Ce-Na₂Mn₃O₇ catalysts are beneficial for permeation of the O₂ and NO/NO₂ reactants as well as enhancing the contact efficiency between soot and catalyst particles.

To reveal the morphological and structural details, TEM and HR-S/TEM images of the catalysts were analyzed (Fig. 1D, F–J, and Fig. S3). The TEM image of Na₂Mn₃O₇ shows that the nanosheets are produced by aggregation of the Na₂Mn₃O₇ nanoparticles with the diameter of 60–100 nm. In addition, some mesopores formed by interparticle voids can also be observed (Fig. 1D). The lattice distance of 0.56 nm corresponds to the (1–10) crystal face of Na₂Mn₃O₇ (insert of Fig. 1D). The survey TEM picture of 1% Ce-Na₂Mn₃O₇ catalyst reveals that the abundant pores can be clearly observed, and the skeleton of the pores is constituted by the interconnected nanoparticles of Ce-Na₂Mn₃O₇ (Fig. 1F). Formation of a developed pore structure in the Ce-Na₂Mn₃O₇ materials may be related to the glucose combustion in the calcination process, which is strongly influenced by the presence of Ce. The gases of CO₂/CO and H₂O generated by the combustion of glucose were released during the calcination process, serving as "gas phase porogeneous agent" that facilitate the development of observed pore structures. Apparently, in despite the presence of glucose, an essentially non-porous Na₂Mn₃O₇ material is formed in the absence of Ce, indicating that this process is catalyzed by Ce species. The results of XRD, SEM and TEM proved that Ce doped layered-type Na₂Mn₃O₇ catalysts with abundant pores were successfully prepared by facile method using glucose as the pore-formation agent. High resolution imaging shows that the Na₂Mn₃O₇ sheets are decorated by tiny CeO₂ crystals (Fig. 1G) of the average size equal to 3–4 nm (see the corresponding histogram in Fig. 1H). The TEM and HAADF images of 1% Ce-Na₂Mn₃O₇ and 10% Ce-Na₂Mn₃O₇ catalysts also proved the presence of CeO₂ nanocrystals, as indicated in Fig. S4. The EDX spectra (Fig. S5) taken from the selected regions of interest (ROI), confirm the chemical nature of the Na₂Mn₃O₇ plates (ROI 1) and the CeO₂ nanocrystals (ROI 2). The ceria nanocrystals are

deposited on the (1–10) facets of the sodium manganese oxide matrix (Fig. 1I). Aberration corrected HAADF/STEM observations allow for an in-depth analysis of the crystallographic structure of the CeO₂ nanoparticles, and reconstruction of their truncated at (101) cuboctahedral shape enclosed by the (100) and (111) facets, via an inverse Wulff construction (Fig. 1J).

The TEM analysis of the catalysts with other Ce doping levels is shown in Fig. S3. The segregation of Ce into CeO₂ occurs already at the low doping level of 0.1% (Fig. S3A–D). The resultant CeO₂ nanocubes spread sparsely on the Na₂Mn₃O₇ plates, as shown in Fig. S3D. With the rising Ce-doping, the porosity of the catalysts increases (Fig. S3A, E, and I). Overlapping of the Na₂Mn₃O₇ plates and their decoration by CeO₂ nanoparticles that becomes more dense are shown in Fig. S3F, J and G, K. The size of CeO₂ crystallites increases because of coalescence and re-entrant growth (Fig. S3 G and K), and their diameter distributions become broader (4–18 nm for 10% and 10–50 nm for 50% Ce doped catalysts, respectively, see Fig. S6). In addition, variation of the shape of CeO₂ crystallites can also be noticed (Fig. S3D, H and L), from nanocubes (for Ce doping of 0.1%) to cuboctahedra (for Ce > 1%). The observed structural and morphological changes of the Ce-Na₂Mn₃O₇ catalysts are in line with the XRD results (Fig. 1A).

In order to more deeply observe the distributions of Ce, Na, Mn and O elements in Ce-Na₂Mn₃O₇, the HAADF-STEM image and EDX elemental mappings of 1% Ce-Na₂Mn₃O₇ under high resolution were tested (Fig. 2A). Na, Mn and O elements have homogeneous distribution as the main components of the 1%Ce-Na₂Mn₃O₇ catalyst. Because of low doping amounts, the mapping of Ce is a challenging task. To sensibly observe the distribution of Ce, the HAADF-STEM image and EDX mapping of Ce were integrated, implying that Ce were atomically distributed in Na₂Mn₃O₇ catalyst. The aberration-corrected HAADF-STEM images also show that some monatomic Ce is present at the edges of Na₂Mn₃O₇ grains (marked by red circle in the Fig. 2B). To verify the existence of monatomic Ce in the Ce-Na₂Mn₃O₇ catalysts, X-ray absorption spectrum (XAS) was employed for the selected 1%Ce-Na₂Mn₃O₇ catalyst (Figs. 2C, 2D). The XANES spectra demonstrate that 1%Ce-Na₂Mn₃O₇ exhibits a sharp single peak located at 5729.8 eV, which is close to the status of Ce³⁺, and markedly different from the two well-separated characteristic peaks of CeO₂ sample (Fig. 2C). These results suggest that Ce may exist in 1%Ce-Na₂Mn₃O₇ as Ce³⁺ in the form of isolated species [60]. Fig. 2D shows the Fourier-transform extended X-ray absorption fine structure spectrum (EXAFS) of 1%Ce-Na₂Mn₃O₇ and CeO₂. Evidently, there is no obvious peak at 3.58 Å in 1%Ce-Na₂Mn₃O₇ catalyst, which is assigned to the Ce-Ce scattering in CeO₂. Wavelet Transform analysis of 1%Ce-Na₂Mn₃O₇ catalyst and CeO₂ sample was also carried out (Figs. 2E, 2F). The catalyst has a Ce-O signal similar to that of CeO₂ sample, yet the Ce-O peak position of 1%Ce-Na₂Mn₃O₇ moves to the lower *k* region, which may be caused by the distinct difference between the Ce configuration of the catalyst and CeO₂. These results imply the presence of the dispersed Ce single atoms in the 1%Ce-Na₂Mn₃O₇ catalyst.

3.2. Redox properties of Ce-Na₂Mn₃O₇ catalysts

To investigate the relationship between the redox properties and the catalytic activities, the synthesized catalysts were tested by H₂-TPR and O₂-TPD (Fig. 3 A, 3B, Table S2 and S3). The H₂-TPR profiles can be fitted into four or five peaks depending on the Ce amount (Fig. 3 A). According to the Ellingham diagram for the manganese oxides, MnO is the final stable phase in the H₂-TPR conditions [61,62,81]. Therefore, the variations of the valence states of Mnⁿ⁺ in manganese oxides are typically associated with the following reduction steps: Mn⁴⁺ → Mn³⁺ → Mn²⁺, corresponding plausibly to gradual transformation: Na₂Mn₃O₇ → Na₂Mn_{3-2δ}Mn³⁺_{2δ}O_{7-δ} → Na_x/Mn₂O₃ → Na_x/Mn_{2-2δ}Mn³⁺_{2δ}O_{3-δ} → Na_x/MnO [55]. The first peak at about 271 °C corresponds to extraction of surface oxygen species and the associated reduction of part of the surface Mn⁴⁺ cations (Na₂Mn₃O₇ → Na₂Mn_{3-2δ}Mn³⁺_{2δ}O_{7-δ}), see Fig. 3Aa and Table S2. The main reduction peak located at about 325 °C is then

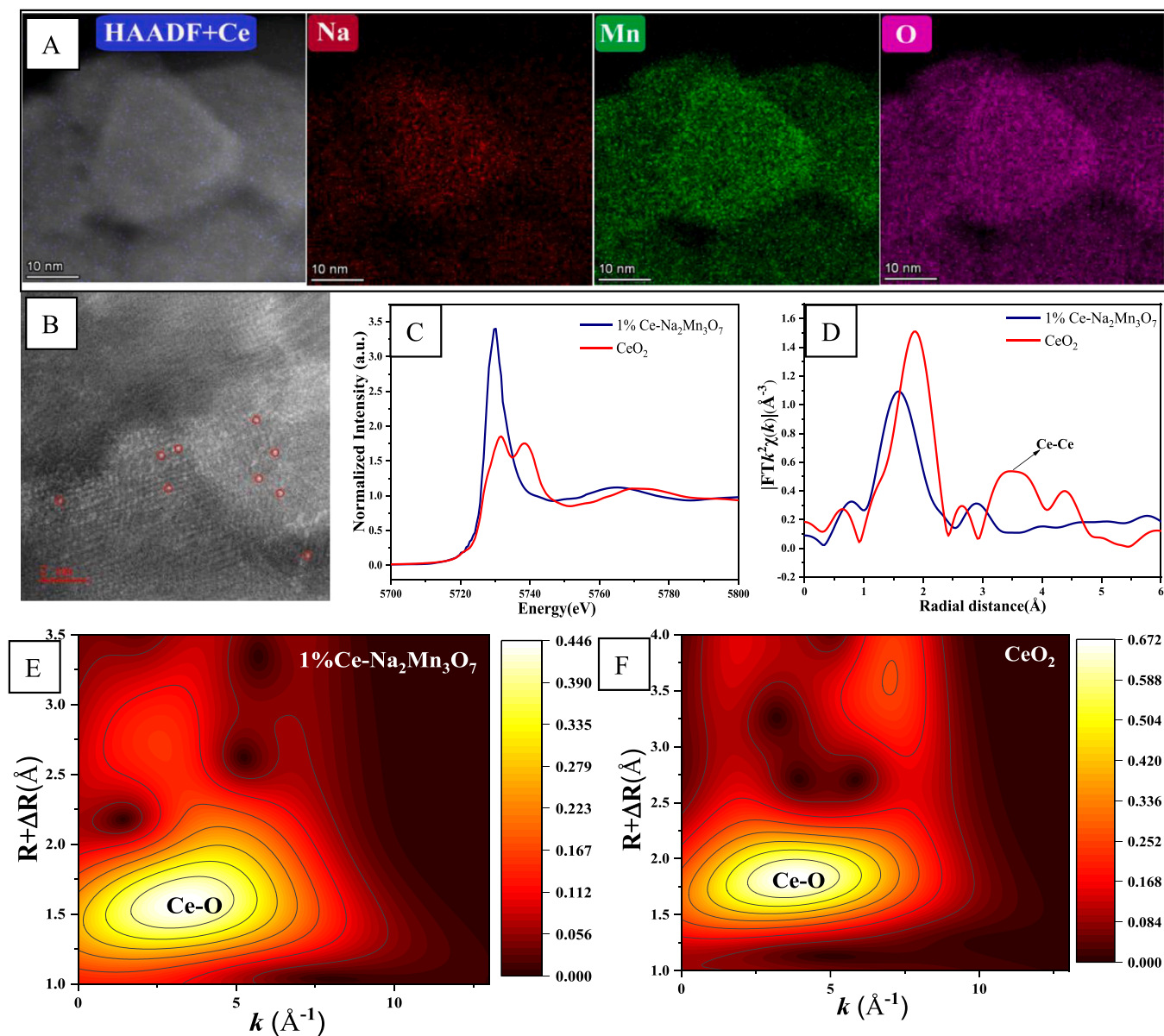


Fig. 2. EDX elemental mapping and HAADF-STEM of 1%Ce-Na₂Mn₃O₇ under high resolution (A), aberration-corrected HAADF-STEM image (B) and EXAFS of 1% Ce-Na₂Mn₃O₇ (C, D), Wavelet Transform analysis of 1%Ce-Na₂Mn₃O₇ catalyst and CeO₂ sample (E, F).

attributed to the reduction of Mn⁴⁺ to Mn³⁺ in the bulk of the catalysts ($\text{Na}_2\text{Mn}_3\text{O}_{7.5} \rightarrow \text{Na}_x/\text{Mn}_2\text{O}_3$), and the peak at ~392 °C to the reduction of Mn³⁺ to Mn²⁺ on the surface of the Na_x/Mn₂O₃ intermediate phase ($\text{Na}_x/\text{Mn}_2\text{O}_3 \rightarrow \text{Na}_x/\text{Mn}_2^{3+}_{10-2\delta}\text{Mn}_2^{2+}_{2\delta}\text{O}_{3.5}$). The fourth reduction peak at 477 °C corresponds to the final bulk reduction of Mn³⁺ into Mn²⁺ ($\text{Na}_x/\text{Mn}_2^{3+}_{10-2\delta}\text{Mn}_2^{2+}_{2\delta}\text{O}_{3.5} \rightarrow \text{Na}_x/\text{MnO}$).

When Ce is doped into the Na₂Mn₃O₇ matrix and/or formed CeO₂ nanoparticles on the surface of Na₂Mn₃O₇, the temperatures of the main reduction peaks are shifted into lower temperatures (Fig. 3 Ab-e). The reduction profiles can be fitted with five peaks when Ce doping is higher than 1%, which is related to the partial reduction of the CeO₂ nanoparticles. In addition, the total H₂ consumption also decreased from 0.460 to 0.111 mmol/g with the increasing of the Ce-doping (Table S2). These results indicate that manganese component of the catalysts is easily reducible, whereas ceria nanoparticles are rather reluctant to reduction, yet modifying the Mn redox behavior in the examined catalysts (see the shifts in the reduction maxima). However, there is an apparent effect of CeO₂ nanoparticles on activation of surface oxygen anions (O²⁻) towards their availability in the soot combustion process.

Indeed, the reduction temperature of Ce-Na₂Mn₃O₇ is shifted down by 20 °C and 40 °C for the surface and bulk species, respectively. Besides that, the position of the CeO₂ reduction peak ($T > 500$ °C) indicates that surface oxygen anions coming from CeO₂ nanoparticles would not take part directly in the soot combustion process (which is accomplished below 400 °C).

As key reactants, various oxygen species play an important role in soot combustion. Therefore, the O₂-TPD profiles for the Ce-Na₂Mn₃O₇ catalysts were determined, and their deconvolution is shown in Fig. 3B. Based on the temperature range of their appearance, three generic kinds of the released oxygen species, denoted as α , β and γ , can be distinguished. The α oxygen present in the temperature range of 50 °C $\leq T \leq 250$ °C can be assigned to dioxygen adspecies attached in the top-on fashion. The β oxygen species desorbing in the temperature range of 250 °C $\leq T \leq 550$ °C corresponds to release of the low coordinated O_{2c}²⁻ and O_{3c}²⁻ surface anions, leading to the formation of the corresponding surface oxygen vacancies in various topographic configurations, as well as to the bridging dioxygen entities. The γ oxygen liberated at the highest temperatures (550 °C $\leq T \leq 850$ °C) are associated with a

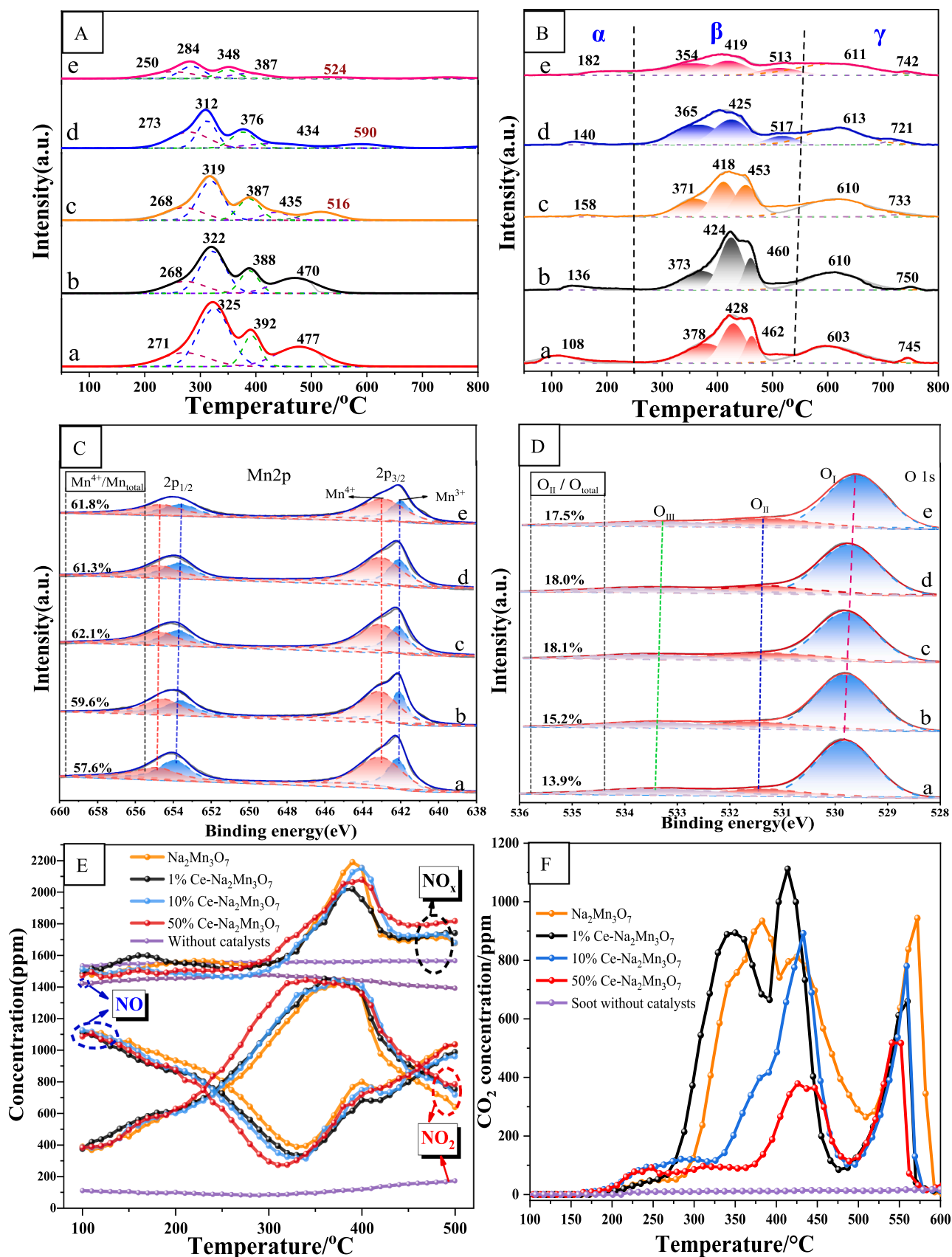
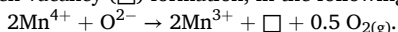


Fig. 3. H₂-TPR (A), O₂-TPD (B), XPS spectra of Mn2p (C) and O1s (D), along with the NO-TPO (E) and soot-TPR (F) profiles (a: $\text{Na}_2\text{Mn}_3\text{O}_7$; b: 0.1% Ce- $\text{Na}_2\text{Mn}_3\text{O}_7$; c: 1% Ce- $\text{Na}_2\text{Mn}_3\text{O}_7$; d: 10% Ce- $\text{Na}_2\text{Mn}_3\text{O}_7$; e: 50% Ce- $\text{Na}_2\text{Mn}_3\text{O}_7$).

deeper bulk release of the lattice oxygen (O^{2-}) of the $Ce-Na_2Mn_3O_7$ catalysts. As shown in Table S3, the β oxygen species are the most abundant for all the catalysts. Combined with the results of the catalytic performance, it can be inferred that the β oxygen species are beneficial for enhancing the catalytic activity, as they are readily available in the temperature range of soot combustion. It is also worth noticing that the relative abundance of all the oxygen species released in the soot combustion window is modified by Ce doping.

Since the composition and valence states of the constituting elements present on the surface have significant influence on the catalytic performance, the XPS measurements of the $Ce-Na_2Mn_3O_7$ catalysts were performed (Fig. 3 C, 3D, Fig. S7 and Table S4). The peaks located at binding energies of 642.3 and 654.1 eV correspond to $Mn\ 2p_{3/2}$ and $Mn\ 2p_{1/2}$, respectively (Fig. 3 C). Because of the proximity in the binding energies of the Mn^{2+} , Mn^{3+} , and Mn^{4+} cations, and broadening of the peaks resulting from the spin multiplicity, it is difficult to reliably distinguish the valence states of Mn based on the standard decomposition of the Mn 2p peaks only. Therefore, the Mn 3s spectra were also recorded, as the energy separation in the Mn 3s spin-orbit doublet, ΔE , was correlated with an average Mn oxidation state (AOS), following the simple empirical relation: $AOS = 8.95 - 1.13 \times \Delta E$ [63]. According to the observed ΔE values, the valence states of Mn in the $Ce-Na_2Mn_3O_7$ catalysts can be attributed to the coexistence of the Mn^{4+} (major contribution) and Mn^{3+} (minor contribution) cations (Fig. S7A and Table S4).

The average oxidation state of Mn cations in the surface region for the bare $Na_2Mn_3O_7$, which was calculated from the relative content of Mn^{3+} and Mn^{4+} cations (3.58), remains in a reasonable agreement with the AOS value determined from the shifts in the Mn 3s XPS spectra (3.62). For the Ce-doped catalysts only a slight increase in the surface AOS values (3.60–3.62 and 3.65–3.7, respectively) was observed. A similar trend in the Mn-AOS was observed in the catalysts bulk, determined from the XAS spectra (Fig. S8), yet the AOS values are distinctly higher and are varying in a narrower range (3.96–3.986). These observations indicate that there are abundant oxygen vacancies on the catalyst surface, leading to deeper reduction of the Mn cations located in the near the surface region, as revealed by XPS. However, the corroborative EPR measurements showed, apart from Mn^{4+} with $S = 3/2$ (broad signal at $g = 2.0$), also the presence of the Mn^{2+} ($S = 5/2$) cations. Their appearance is easily recognized by the observed characteristic sextet hyperfine structure ($I = 5/2$, $A/g = 9.5\ mT$), the intensity of which increases greatly with the Ce loading amount (Fig. S9). The XPS results imply that some of the Mn^{4+} cations are reduced into Mn^{3+} due to oxygen vacancy (\square) formation, in the following way:



Such reduction is typically reported for the high valent Mn^{4+} cations in oxides [29,64]. The EPR spectra show, in turn, that part of the Mn^{3+} may disproportionate into Mn^{2+} and Mn^{4+} and/or be reduced deeper to Mn^{2+} , which is distinctly favored by the high Ce loading (10% and 50%), in line with an easier reduction of $Ce-Na_2Mn_3O_7$ observed in the H_2 -TPR experiments. These findings imply that there is a considerable indirect redox interaction between the $Na_2Mn_3O_7$ and Ce ions/ CeO_2 moieties that promotes appreciable reduction of the manganese cations, which is beneficial for dioxygen activation.

The XPS spectra of Ce 3d shown in Fig. S7B can be fitted with eight peaks corresponding to four pairs of the spin-orbit doublets. The peaks labeled as u'' , u' , u and v'' , v' , v are assigned to $Ce^{4+}\ 3d_{3/2}$ and $Ce^{4+}\ 3d_{5/2}$, respectively, whereas the u' and v' peaks are assigned to $Ce^{3+}\ 3d_{3/2}$ and $Ce^{3+}\ 3d_{5/2}$, respectively [65,66]. Unfortunately, acceptable XPS spectra of the diagnostic Ce 3d range can only be obtained when the doping of Ce is higher than 10%. Additionally, the oxidation state of bulk Ce cations for selected samples was determined by XAS spectroscopy (Fig. S8). The obtained AOS values of 3.97, 3.92 and 3.8 for the 1%, 10% and 50% $Ce-Na_2Mn_3O_7$ catalysts, respectively, indicate that gradual partial reduction of ceria takes place as its loading increases. Formation of Ce^{3+} may be assigned to oxygen vacancy formation in the CeO_2 nanocrystals, in an analogous way as for $Na_2Mn_3O_7$. Probably, it

may occur in the interface region, preferentially.

Fig. 3D shows the O 1s XPS spectra of the catalysts. Three kinds of O species, which are labeled as O_I , O_{II} , and O_{III} , can be distinguished by fitting the O 1s peaks observed in the XPS spectra [27,67]. Based on the previous reports and the characteristic binding energies, the O_I signal at $\sim 529.8\ eV$ is ascribed to lattice oxygen, forming the bonds of the type Mn-O, Ce-O and Ce-O-Mn. With the increasing Ce doping, the BE of the O_I species are slightly increased. The O_{II} signal located at BE of $\sim 531.5\ eV$ is related to chemically adsorbed oxygen (such as O_2^- and O^-), and the O_{III} component located at $\sim 533.4\ eV$ may include contributions from hydroxyls present on the surface of $Na_2Mn_3O_7$. The fraction of the O_{II} species initially increased and then decreased with the increasing Ce content, reaching the maximum values for 1% $Ce-Na_2Mn_3O_7$, which is in line with the O_2 -TPD results. (Table S4).

Based on the catalytic performance of the $Ce-Na_2Mn_3O_7$ catalysts under different NO concentrations, it is clear that NO enhances the soot oxidation catalytic activity. To identify the temperature range of NO oxidation into NO_2 over the $Ce-Na_2Mn_3O_7$ catalysts, the NO-TPD profiles were measured (Fig. 3E). The NO_2 formation over the $Ce-Na_2Mn_3O_7$ catalysts significantly increased at first and then decreased with the temperature by reason of approaching the thermodynamic limit. The maximum of the NO_2 production is observed from 300 to 400 °C, and the corresponding NO concentration profile is inverted, confirming that NO_2 is produced at its expense. The NO_x (total nitric oxides) concentrations for all the catalysts exhibit a notable enhancement at the temperature range of 300–400 °C, which indicates that the catalysts have the ability of storage nitric oxides at low temperature and release them at higher temperatures. This point is corroborated by the results of the DFT modeling, described below. Notably, in the reference experiment without the catalyst, NO_2 is not produced in the whole temperature range of the soot oxidation reaction (Fig. 3E). Soot particles that do not in a direct contact with the catalyst's surface are preferentially oxidized by a large amount of NO_2 generated in the presence of the catalyst, rather than by O_2 . The pronounced porosity of the Ce-doped catalysts is then crucial for efficient NO_2 transport from the catalyst surface to soot particles. Furthermore, owing to the high activity of the $Ce-Na_2Mn_3O_7$ catalysts, the soot combustion takes place within the thermodynamically stable temperature window of NO_2 , which is advantageous for its corroborative involvement in this process.

As for all deep oxidation reactions, the amount and straightforward availability of reactive oxygen species are also crucial for soot combustion. In an anoxic soot-TPR reaction, the soot particles can only react with lattice oxygen anions of the catalysts. Therefore, their participation can be differentiated and quantitatively assessed through the CO_2 production analysis [68,69]. Taking soot as a reductant, direct information about the catalysts performance can be obtained. From the deconvolution of the soot-TPR profiles recorded for the $Ce-Na_2Mn_3O_7$ catalysts, the amounts of the particular type of the oxygen anions available for the stoichiometric soot oxidation were calculated (see Fig. 3 F, Fig. S10 and Table S5). It can be readily noticed that the combustion reaction occurs in four stages. The peak positions and the corresponding quantities of the evolving CO_2 are different, varying apparently with the Ce-doping. The onset of the soot oxidation appears already at $\sim 170\ ^\circ C$ (weak peak), and is followed by strong CO_2 peak, shifting its maximum from $\sim 325\ ^\circ C$ to $\sim 450\ ^\circ C$, which is distinctly influenced by ceria. For the samples of the highest Ce loadings (10% and 50%), the second and the third CO_2 peaks are merging. Furthermore, the aerobic soot oxidation is fully accomplished below 450 °C, whereas it extends to 600 °C in the case of the anoxic oxidation. These results indicate that lattice oxygen species can be involved in soot oxidation already at low temperatures (200–350 °C), and that $Ce-Na_2Mn_3O_7$ catalysts with a doping amount of less than 1% is modified by the two states of Ce single atoms and CeO_2 clusters, which is conducive to the activation of oxygen species. The excessive decoration of $Na_2Mn_3O_7$ by CeO_2 is likely to be detrimental to the mutual contact between soot particles and $Na_2Mn_3O_7$ plates, resulting in no further improvement of

the soot oxidation. Yet, the redox behavior of the latter is distinctly enhanced at the low CeO₂ loading (1%). The fact that the soot oxidation process is remarkably changed in the presence of oxygen, indicates that the released lattice oxygen species are readily replaced by the gaseous O₂, keeping the full combustion in the favorable low temperature region ($T < 450$ °C).

By combining the results of the O₂-TPD, H₂-TPR and soot-TPR reference experiments, it is apparent that the catalytic soot oxidation may involve all kinds of oxygen species, namely adsorbed oxygen (stable at $T < 280$ °C), surface oxygen ($280 < T < 500$ °C) and bulk lattice oxygen anions ($T > 500$ °C). These oxygen species may participate in a parallel-consecutive fashion under real soot oxidation conditions, as shown recently by us based on isotopic investigations [29]. The total amounts of oxygen species participating in the soot combustion decrease substantially with the rising Ce doping, which implies that the oxygen

species associated with the Na₂Mn₃O₇ moiety are primarily responsible for soot oxidation. Those results revealed also that the Ce-doping enhances the availability of the surface-active oxygen, in agreement with the results of O₂-TPD and H₂-TPR. As mentioned before, the temperature of complete combustion of soot is lower than 400 °C. Therefore, the reactive oxygen species (ROS) appearing at < 400 °C, have significant influence on the catalytic performance. The ROS fractions for Na₂Mn₃O₇, 1% Ce-Na₂Mn₃O₇, 10% Ce-Na₂Mn₃O₇ and 50% Ce-Na₂Mn₃O₇ are equal to 30.3%, 51.2%, 35.2% and 23.4%, with the corresponding total amounts of 1.08×10^{-4} , 1.65×10^{-4} , 0.72×10^{-4} and 0.32×10^{-4} mol·g⁻¹, respectively (Table S5). The ROS amounts for 1% Ce-Na₂Mn₃O₇ is the highest among the catalysts, which implies the excellent catalytic performance of this sample.

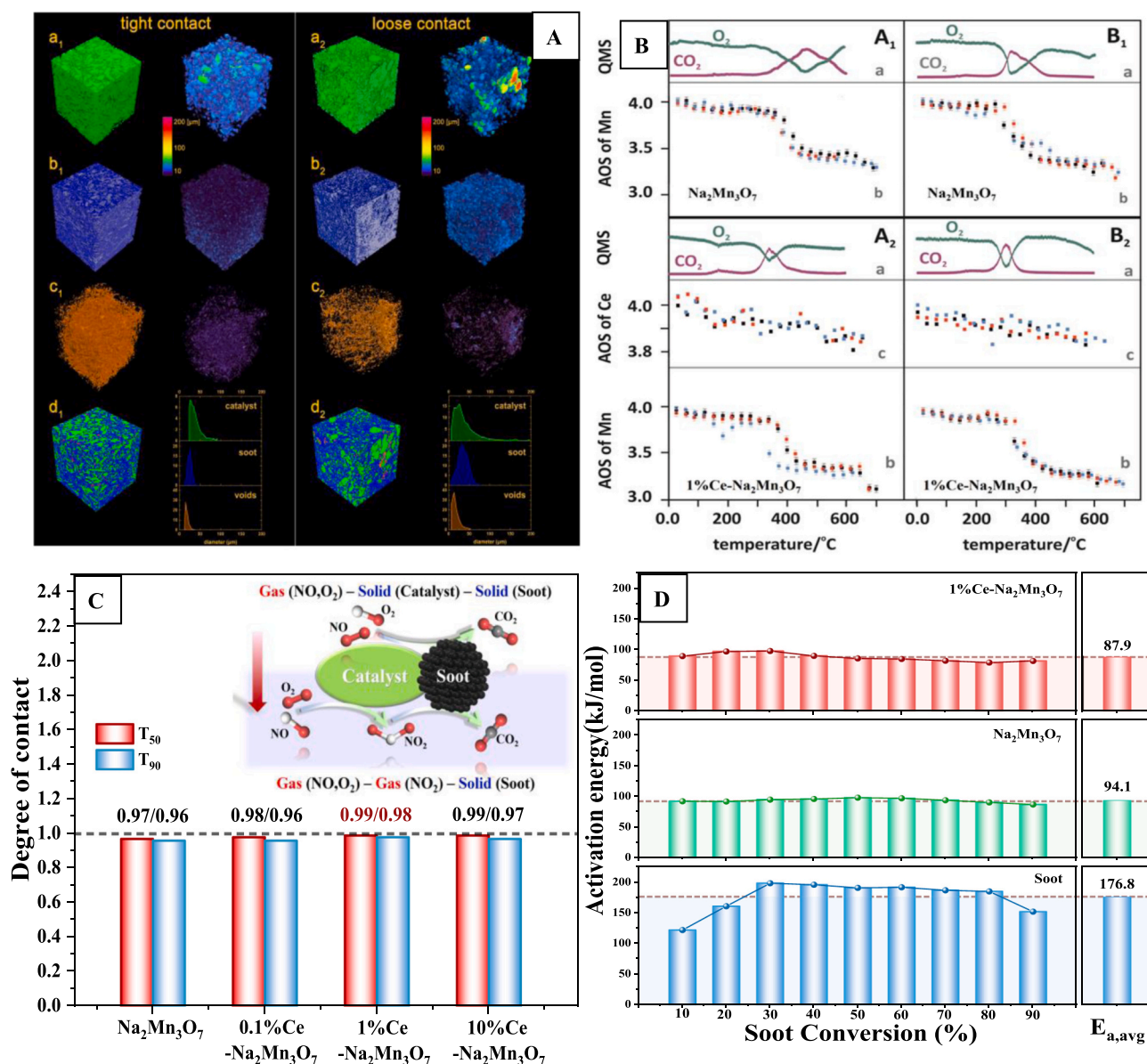


Fig. 4. Mutual arrangement of soot and catalyst particles (A), redox behavior of the Mn and Ce cations of the Na₂Mn₃O₇ and 1% Ce-Na₂Mn₃O₇ catalysts during soot combustion (B), the contact efficiency calculated based on the T₅₀ and T₉₀ values for Ce-Na₂Mn₃O₇ catalysts, insert represents a schematic diagram of the transformation of reaction mechanism (C) and the activation energy of the catalysts for soot conversion under loose contact mode (D). In Fig. 4A, spatial distribution of the catalyst (a₁, a₂), soot particles (b₁, b₂), empty voids (c₁, c₂), imaging of the whole ensemble (d₁, d₂) in the TC and LC modes, along with the corresponding size color coded 3D models (right side), and the histograms. In Fig. 4B, the QMS profiles of O₂ and CO₂ (a), and average oxidation state of Mn (b) and Ce (c) cations under the presence of O₂ (A₁, A₂), or O₂ and NO (B₁, B₂) during soot combustion, red dots for LC mode, blue dots for TC mode, and black dots for test without soot).

3.3. Identifying the main factors governing the soot oxidation activity

Besides the intrinsic activity of the catalysts, described above, contact efficiency between the catalyst and soot particles is also an important factor for interpretation of the catalytic performance. Generally, the tight contact (TC) mode maximizes the number of the contact points (dense packing), while in the loose contact (LC) mode the corresponding numbers are lower, but closer to those appearing in the conditions of real applications. Therefore, when the activities under the tight and loose combustion modes are similar, the catalysts exhibit high contact efficiency with the soot particles, which is promising for their future applications. Except of their intimate contact, arrangement of the soot and catalysts grains plays also an important role, governing the efficiency of heat transfer in the micrometric scale. Since the number of the mutual contacts is gradually decreasing with the combustion progress, the autogenously produced heat is then essential for enhancing the local temperature, which is beneficial for sustaining the reaction (afterburning stage).

The micrometric scale imaging of mutual arrangement for the soot and the catalyst's particles under TC and LC modes was examined by means of the X-ray microtomography, and the results are shown in Fig. 4 A. Based on the micrometric resolution of the μ -CT technique, the nanometric features of the $\text{Na}_2\text{Mn}_3\text{O}_7$ plates observed in TEM (see Fig. 1D) are smeared out, and only their agglomerates (grains) are well revealed. The distributions of the catalyst and soot particles in the selected submillimetric volume of interest (VOI), as well as the empty space between them are shown in Fig. 4Aa₁, Ab₁, Ac₁ for TC and Aa₂, Ab₂, Ac₂ for LC, respectively. In Fig. 4Ad₁ and Ad₂, all the determined spatial arrangements are superimposed, illustrating the formation of a compact catalyst-soot assembly. The catalyst and the soot particles are gathered into micrometric grains of a quite uniform size dispersion (centered around 25 μm), whereas the voids are smaller with a narrower dispersion ($\sim 15 \mu\text{m}$), as shown in the corresponding histograms. This is also reflected in an alternative way in the volume-rendered models shown on the right sides.

In the TC mode, the catalyst grains are surrounded by the tightly packed soot particles (Fig. 4Ad₁), leaving small empty voids only (Fig. 4Ac₁). The latter are quite homogeneously distributed throughout the analyzed VOI. The soot particles, which are not in a mutual contact with the catalyst are densely packed. In the LC mode, the overall packing of the soot and the catalyst particles is similar in comparison to that observed in the tight contact (Fig. 4Aa₂-d₂), but appreciably more heterogeneous. Indeed, the catalyst and soot grains exhibit broader size distributions, but the intermingling of the soot with the catalyst is slightly less efficient than in the TC mode (Fig. 4Ad₁ and d₂). The empty spaces are, however, of similar average size, tailing toward larger values. In conclusion, at the micrometric scale, both the TC and LC packing modes result in the formation of rather similar compact catalyst-soot assemblies with a minor fraction of the voids, which is favorable for a good heat transfer allowing for an efficient afterburning.

Direct intimate contact between the catalyst and soot nanoparticles plays a crucial role, particularly at the initial stages of the soot combustion where the temperature is low. The degree of relative contact (DRC), was assessed based on the T_{50} and T_{90} values, determined under tight contact (TC) and loose contact mode (LC), as shown in Fig. 4 C and Table S6. The DRC values are associated with the contact between soot and catalyst, thus higher DRC values represent more effective transfer of the adsorbed and surface oxygen species from the catalyst to soot [70]. The DRC values of the $\text{Ce-Na}_2\text{Mn}_3\text{O}_7$ catalysts are close to 1 (Fig. 4 C). The soot conversions in the loose and tight contact modes were similar with each other, especially for the T_{50} and T_{90} values (Fig. S11). Combined the results of NO-TPO, and the catalytic activity of $\text{Ce-Na}_2\text{Mn}_3\text{O}_7$ catalyst under different NO concentrations, the DRC values once again demonstrate that the reaction pathway of soot combustion has been changed from the way of "gas-solid-solid" to the "gas-gas-solid" due to the efficient production of NO_2 , as is clearly illustrated in the insert of

Fig. 4 C. All these results illustrate that the $\text{Ce-Na}_2\text{Mn}_3\text{O}_7$ catalyst with the abundant and readily available ROS (Reactive oxygen species), high NO to NO_2 oxidation capacity and developed pore structure, all of which are favored by the presence of Ce and become a promising candidate for practical applications.

The oxidation state of manganese is distinctly influenced by the redox character of soot combustion. The region of particular interest is the temperature window 250–450 °C, where the soot oxidation takes place. To follow the redox behavior of the $\text{Na}_2\text{Mn}_3\text{O}_7$ and $\text{Ce-Na}_2\text{Mn}_3\text{O}_7$ catalysts during the soot combustion, we performed operando XAS measurements in the flow of 5% O_2/He , and 5% $\text{O}_2/1\%\text{NO}/\text{He}$ in the presence of soot in both TC and LC modes, and in the absence soot as a reference. The corresponding evolution of the average oxidation state of Mn cations during the soot combustion at various reaction conditions are presented in Fig. 4B. At the first stage of the combustion in O_2 (till $\sim 300^\circ\text{C}$), the changes in the manganese AOS values are rather small for both bare and Ce-doped catalysts. A sudden drop of AOS (from 3.965 to 3.43 and 3.96–3.48, for $\text{Na}_2\text{Mn}_3\text{O}_7$ and $\text{Ce-Na}_2\text{Mn}_3\text{O}_7$, respectively) can be observed in the range of 300–450 °C (Fig. 4BA₁b, BB₁b, BA₂b, BB₂b), and is well correlated with the soot combustion. The observed decrease of the Mn-AOS values is consistent with the loss of the surface oxygen species (see the broad β band in O_2 -TPD), which apparently takes part in the soot oxidation, (along with the adsorbed reactive oxygen species). The catalysts surface becomes defected due to the oxygen vacancy formation, and then becomes virtually stable (above 500 °C), maintaining the Mn average oxidation state in the range of 3.43 – 3.48 in the flow of O_2 . In the presence of NO in the reaction mixture, the changes in the average oxidation state of manganese are shifted to lower temperatures (250 °C), confirming the positive effect of nitric oxide on the soot combustion. The drop of the Mn-AOS values is slightly higher (to 3.35–3.36), and appreciably affected by the Ce-doping. This finding illustrates that NO can also be oxidized into NO_2 by the surface $\text{O}_2^{\cdot-}$ and $\text{O}_3^{\cdot-}$ anions, which can be inferred from the comparison of the AOS profiles with and without NO in the absence of soot. Another feature revealed by the operando XAS investigations is that the AOS profiles of Mn for both TC and LC modes of the combustion without NO tend to be situated slightly below the corresponding Mn-AOS profile without soot, which is most distinctly manifested for the soot oxidation in TC mode over the 1% $\text{Ce-Na}_2\text{Mn}_3\text{O}_7$ catalyst (Fig. 4BA₁b). However, when NO is present all Mn-AOS curves become practically amalgamated. These observations indicate that the surface $\text{O}_2^{\cdot-}$ and $\text{O}_3^{\cdot-}$ anions lost during soot oxidation can be promptly replenished by incorporation of dioxygen, allowing for the combustion process to turn-over sustainably. Merging of the Mn-AOS profiles when NO is present, remains in line with the fact that it may be oxidized by the readily available $\text{O}_2^{\cdot-}$ and $\text{O}_3^{\cdot-}$ anions (in accordance with IR studies, see below). Comparison of the Mn-AOS profiles for $\text{Na}_2\text{Mn}_3\text{O}_7$ and 1% $\text{Ce-Na}_2\text{Mn}_3\text{O}_7$ with the corresponding profiles of the CO_2 and O_2 evolution, shows clearly that substantial reduction of Mn occurs in the late stage of the soot combustion in O_2 , but when NO is present it occurs concomitantly with the soot oxidation. In contrast to the Mn-AOS values, the changes in the average oxidation state of Ce are distinctly smaller, and are apparently not correlated with the Mn-AOS drop during the soot oxidation progress. The Ce-AOS values decrease rather steadily to ~ 3.9 at the end of the combustion process, virtually regardless the feed composition (Fig. 4BB₁c, 4BB₂c). Interestingly, doping with Ce narrows significantly the temperature range of soot oxidation, and slightly increases the drop of the Mn-AOS values, which implies that the combustion process occurs in a harsher fashion.

These observations confirm that the temperature gap between the loose and tight contacts is successfully bridged by the developed $\text{Ce-Na}_2\text{Mn}_3\text{O}_7$ catalysts, owing to their unique redox properties (intrinsic lability of surface oxygen species and their efficient replenishment by gaseous O_2 , which are not perturbed appreciably by the soot oxidation process). This reveals a facile redox auto-tuning of the $\text{Na}_2\text{Mn}_3\text{O}_7$ and $\text{Ce-Na}_2\text{Mn}_3\text{O}_7$ catalysts to the actual reaction conditions, even when the oxygen species are extensively drained with the progress of the soot

combustion. Although, there is apparently no direct coupling between the redox behavior of the Mn and Ce cations, the presence of Ce shifts significantly the late stage of the reaction to lower temperatures (Fig. 4BA₁a, BA₂a and BB₁a, BB₂a). As a result, the combustion reaction occurs at low temperatures, where the produced NO₂ is thermodynamically stable. Thus, NO₂ can be exploited effectively for oxidation of remote soot particles during the whole combustion process. Furthermore, the fact that in the presence of NO the significant changes of Mn-AOS take place over the entire temperature region of the soot combustion, is consistent with NO oxidation into NO₂ not only by the adsorbed oxygen, but also by the lattice O_{2c}/O_{3c} oxygen (see below).

The intrinsic activity of catalysts is also one of the basic factors in heterogeneous catalytic reactions. To confirm the effect of Ce doping on the intrinsic activity of soot combustion, the apparent activation

energies (E_a) for the Na₂Mn₃O₇ and 1% Ce-Na₂Mn₃O₇ catalysts at soot conversions of 10–90%, calculated from the variable heating rate experiments using the Arrhenius method [71], as shown in Fig. 4D. To sensibly compare the changes in the activation energy, the average values, $\langle E_a \rangle$, calculated from the E_a values obtained under different soot conversions were applied as a simple index of the catalytic performance [72]. The $\langle E_a \rangle$ value of the noncatalytic soot combustion, equal to 176.8 kJ/mol, is close to those reported for bare soot combustion [73]. When the catalysts are present, the $\langle E_a \rangle$ values dramatically decline to 94.1 kJ/mol and 87.9 kJ/mol for the undoped Na₂Mn₃O₇ and 1% Ce-Na₂Mn₃O₇ catalysts, respectively. The doping with Ce reduces the energy barrier and promotes soot combustion, implying that the Ce-Na₂Mn₃O₇ catalysts will exhibit a better activity for soot oxidation than the Na₂Mn₃O₇ catalyst.

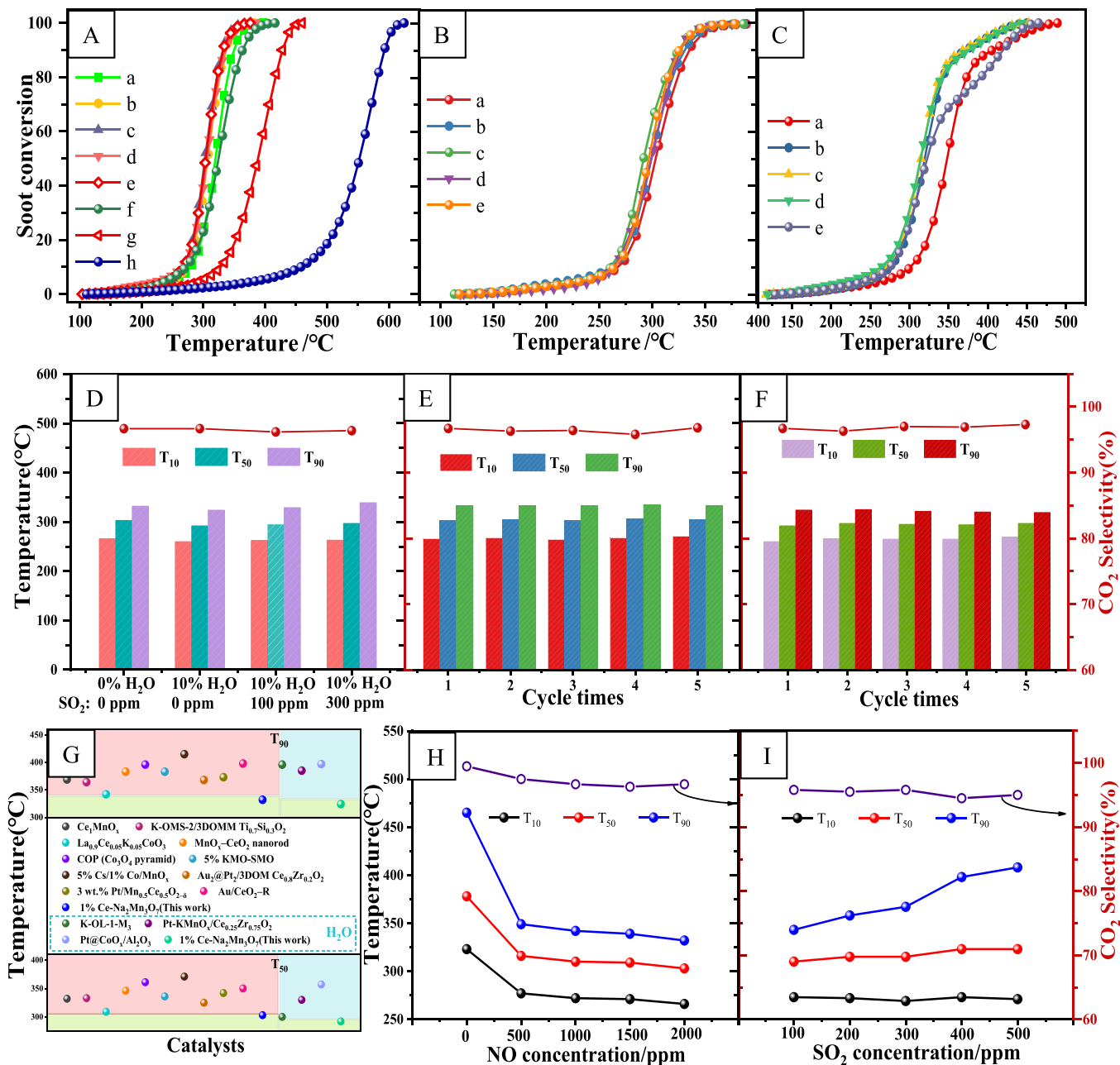


Fig. 5. Catalytic performance of as-prepared catalysts for soot combustion under different reaction conditions (A: 10% O₂ + 0.2% NO + Ar balance; B: 10% O₂ + 0.2% NO + 10% H₂O + Ar balance; C: 10% O₂ + 0.2% NO + 300 ppm SO₂ + Ar balance), tolerance to sulfur dioxide and water (D), the stability under the presence of 10% H₂O (F), comparison for T₅₀ and T₉₀ values of 1%Ce-Na₂Mn₃O₇ and reported catalysts (G), the catalytic performance under different NO (H) and SO₂ concentrations (I) (a: Na₂Mn₃O₇; b: 0.1%Ce-Na₂Mn₃O₇; c: 1% Ce-Na₂Mn₃O₇; d: 10% Ce-Na₂Mn₃O₇; e: 50% Ce-Na₂Mn₃O₇; f: MnO_x; g: CeO₂; h: bare soot).

3.4. Catalytic performance of Ce-Na₂Mn₃O₇ catalysts in soot combustion

The performance of the Ce-Na₂Mn₃O₇ catalysts for soot combustion was evaluated under various reaction conditions, and the obtained results are collated in Fig. 5. The conversion profiles of soot combustion under the reaction atmosphere of 10% O₂, 0.2% NO and Ar balance are shown in Fig. 5 A. The corresponding T_{10} , T_{50} , and T_{90} values and CO₂ selectivity are listed in Table S7. To illustrate the catalytic performance, combustion of bare soot (without catalyst) was tested under the same reaction conditions. It can readily be observed that the soot conversion profiles are strongly moved to low temperatures when the catalysts are present (Fig. 5 A). Whereas the T_{10} , T_{50} , and T_{90} values of the bare soot combustion were equal to 458 °C, 551 °C, and 594 °C, respectively (Table S7). The values are dramatically decreased in the case of the catalytic combustion (below 400 °C), indicating an excellent catalytic performance of the synthesized materials. Interestingly, the Ce-doping of Na₂Mn₃O₇ has a significant influence on the catalytic activity, even at the amount of only 0.05% (mole ratio of Ce:Mn). The high catalytic activity of the Ce-Na₂Mn₃O₇ catalysts is maintained even if the Ce-doping reaches the level up to 50%. The 1% Ce-Na₂Mn₃O₇ catalyst exhibited apparently the highest catalytic activity with the spectacular T_{10} , T_{50} , and T_{90} values of 266 °C, 303 °C, and 332 °C (Table S7) and the Ce-Na₂Mn₃O₇ catalysts show high CO₂ selectivity, exceeding 94% in all experiments. To investigate the synergistic effects of Ce, Na and Mn, the catalytic performance of the reference 50%Na-CeO₂, 1%Ce-MnO_x, MnO_x and CeO₂ materials were also evaluated (Fig. 5 A and Table S7). The apparent lower catalytic activities of the reference systems, than those of the layered Ce-Na₂Mn₃O₇ catalysts, suggests that the synergistic effect between Ce, Na and Mn plays an important role in the soot combustion.

The sulfur compounds and water vapor are unavoidable in combustion of diesel oil and are ubiquitous in diesel engine exhausts. To satisfy the requirements of practical applications, the catalytic performances of the Ce-Na₂Mn₃O₇ catalysts under water vapor (10%) and SO₂ (300 ppm) were evaluated (Figs. 5B, 5 C, Table S8 and S9). When water vapor was introduced, the activities of all the catalysts are slightly enhanced, which is consistent with previous reports [74,75]. In such conditions, 5%Ce-Na₂Mn₃O₇ exhibits the highest catalytic activity among the examined catalysts, with the T_{10} , T_{50} , and T_{90} values of 261 °C, 291 °C, and 321 °C. This is also the best catalytic activity for thermal catalytic soot combustion in the medium and high temperature ranges, among those reported in the literature [76–80]. The reasons for the excellent activity under water vapor can be related with the formation of protonated species (such as HNO₃) or lowering of the activation energy [81]. Meantime, water vapor may form a thermal conductive layer around soot particles and catalysts, and the water-derived oxygen species (e.g., hydroxyls) on the catalyst surface accelerate the reaction by interacting with soot directly [82]. When SO₂ was introduced, the activities of all the catalysts are slightly decreased (Fig. 5 C and Table S9). The observed changes in the catalytic activities are apparently different at the T_{10} , T_{50} , and T_{90} temperatures, compared to those obtained in the absence of SO₂. Whereas the values of T_{10} are barely changed, the T_{50} values increase by about 10 °C for all the Ce-Na₂Mn₃O₇ catalysts. However, the strongest effect takes place for the T_{90} values, which increase by about 30–50 °C under 300 ppm of SO₂, for all the catalysts. The tendency to grow of the T_{10} , T_{50} , and T_{90} values for the bare Na₂Mn₃O₇ catalyst is larger than that for the Ce-Na₂Mn₃O₇ catalysts (Table S9). These observations indicate directly that the doping of Na₂Mn₃O₇ with Ce is beneficial for enhancing the sulfur resistance [83]. Due to the simultaneous presence of sulfur compounds and water vapor in diesel engine exhausts, the catalytic performance of the 1% Ce-Na₂Mn₃O₇ catalyst under different SO₂ concentrations and H₂O (10%) were tested (Fig. 5D and Table S10), exhibiting similar activity to that measured for 10% H₂O only. The SO₂ concentration has almost no influence on the catalytic activity when both SO₂ (300 ppm) and water vapor (10%) were present in the reaction gases. These results augur well for practical applications of Ce-Na₂Mn₃O₇ as a promising active phase of

the CDPF systems.

Beside the influence of SO₂ and water vapor, the operational durability is another important factor for catalysts when they are designed for future practical applications. Therefore, the catalytic performance of the 1% Ce-Na₂Mn₃O₇ catalyst were tested in a recyclable fashion under different reaction atmospheres (Figs. 5E, 5 F, Table S11 and S12). When water vapor was absent in the reaction gases, the catalyst exhibits good stability, even when used 5 times. The observed variations of the T_{10} , T_{50} , and T_{90} values are quite small and equal to 265 °C ± 5 °C, 304 °C ± 2 °C, and 333 °C ± 2 °C, respectively (Fig. 5E and Table S11). At the same time, the CO₂ selectivities were all higher than 95%. When water vapor was introduced, the 1% Ce-Na₂Mn₃O₇ catalyst preserves its good stability, with the T_{10} , T_{50} , and T_{90} values being 265 °C ± 5 °C, 295 °C ± 3 °C, and 322 °C ± 3 °C, respectively, for the 5 consecutive cycles. More importantly, it should be noted that the catalytic activities of the Ce-Na₂Mn₃O₇ catalysts are higher than those reported so far (including noble metal catalysts) in the medium and high temperature ranges, whether the reaction atmosphere contains water or not (Fig. 5 G and Table S15).

It is well known that NO_x and soot particles are produced in a “trade-off” fashion in diesel engines. To investigate the influence of NO, the catalytic activities of the 1% Ce-Na₂Mn₃O₇ catalyst were tested under different NO concentrations (Fig. 5H and Table S13). When NO was absent, the T_{10} , T_{50} , and T_{90} values were equal to 323 °C, 378 °C, and 465 °C, respectively. The catalytic activity of the 1% Ce-Na₂Mn₃O₇ catalyst is greatly enhanced when NO was introduced, even at the level of 500 ppm, and the T_{10} , T_{50} , and T_{90} values drop markedly to 277 °C, 316 °C and 349 °C, respectively. With an increasing NO concentration, the catalytic activity is further only slightly improved. These results indicate that NO is an important reactant for improving the catalytic activity of the Ce-Na₂Mn₃O₇ catalysts, yet acting positively to the certain level only. Based on previous reports, NO can firstly be converted into NO₂ owing to strong oxidation ability of the catalysts. Then, NO₂ acting as an oxygen carrier, directly reacts with soot particles, switching the reaction pathway from the less efficient “gas-solid-solid” into the more favorable “gas-gas-solid”, greatly enhancing the contact efficiency between the soot and the catalyst particles, thereby [18,84,85]. In addition, the NO concentration exhibited a weak influence on CO₂ selectivity, which remained higher than 98% for different NO concentrations. As mentioned before, sulfur compound is also another unavoidable pollutant in the exhaust gases that can easily lead to poisoning of the catalysts. To evaluate the sulfur resistance of the synthesized materials in more detail, the catalytic activities of the 1% Ce-Na₂Mn₃O₇ catalyst were also examined under different SO₂ concentrations (Fig. 5I and Table S14). The measured activity dropped when SO₂ was introduced into the reaction gases, and steadily decreased with the increasing of SO₂ concentration. However, whereas the T_{10} values remain essentially constant, the T_{90} values significantly increase with the growing SO₂ concentrations. The reasons for such behavior may be related to the fact that some active sites were poisoned by sulfur, under high reaction temperature at high SO₂ levels. However, with the increasingly stringent new fuel standards, the SO₂ concentration should be pushed well below the 10 ppm level of the current requirements. Therefore, the developed Ce-Na₂Mn₃O₇ catalysts can still be considered as one of the most promising candidates for practical applications.

3.5. Reaction mechanisms of soot combustion on Ce-Na₂Mn₃O₇ catalysts

To provide a molecular insight into the interaction of NO with the catalyst surface in the presence of O₂, in-situ DRIFTS measurements for the 1% Ce-Na₂Mn₃O₇ catalyst under different atmosphere conditions were carried out (Fig. 6 A and 6B). Multiple bands in the region of 2000–1000 cm^{−1} were observed at different temperatures. When the reaction atmosphere corresponds to 2000 ppm NO and 10% O₂ (Fig. 6 A), multiple adsorbed species may correspond to monodentate nitrate (1016 cm^{−1}), ionic nitrate (1381 cm^{−1}), nitro compounds

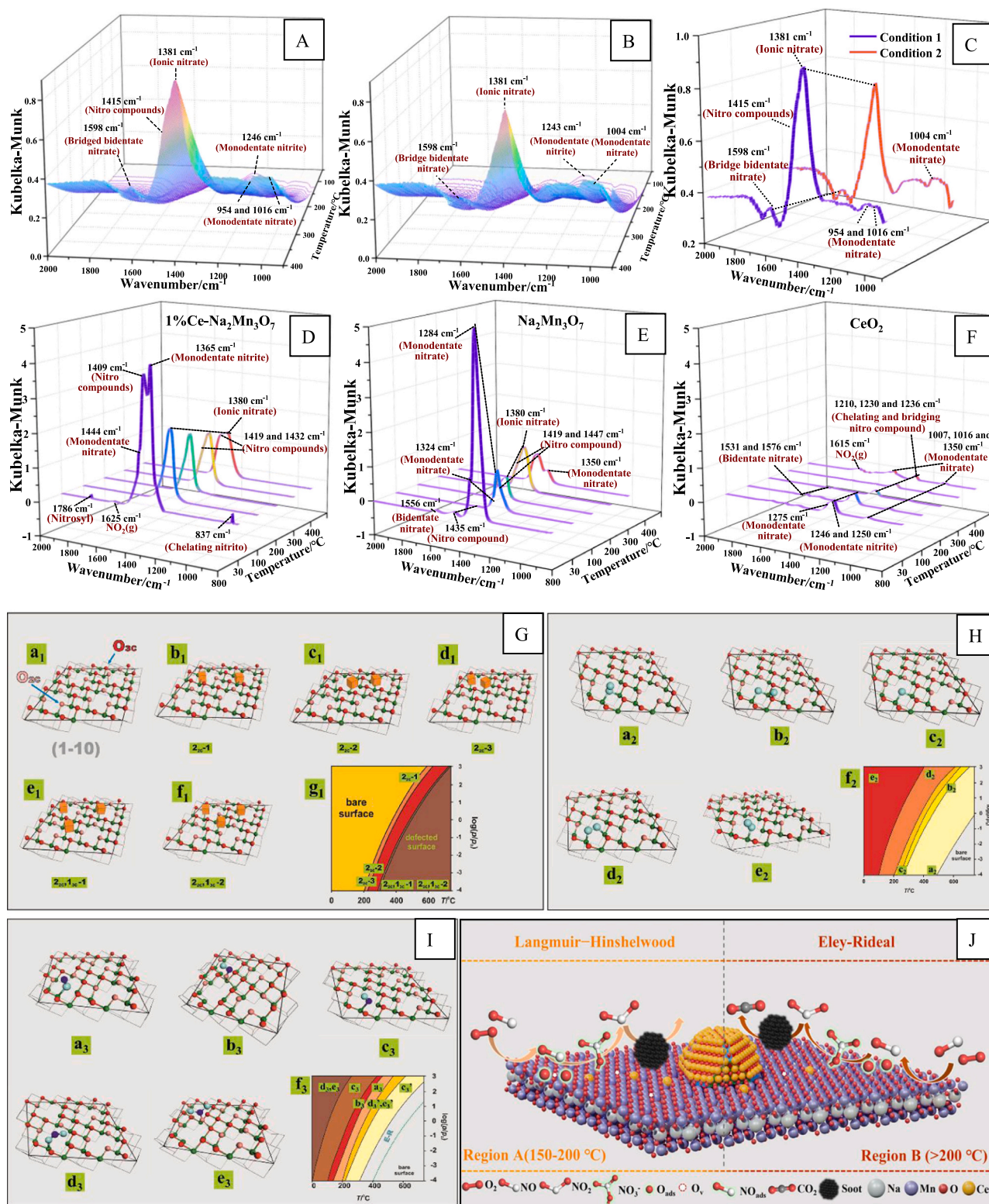


Fig. 6. In-situ DRIFT spectra of soot oxidation carried out over 1% Ce-Na₂Mn₃O₇ catalyst under conditions of 2000 ppm NO + 10% O₂ + Ar balance (A, Condition 1), 2000 ppm NO + Ar balance (B, Condition 2). The comparative spectra under 400 °C for Conditions 1 and 2 for 1% Ce-Na₂Mn₃O₇ catalyst (C). In-situ isothermal DRIFT spectra of NO_x adsorption (2000 ppm NO + 10% O₂) on 1% Ce-Na₂Mn₃O₇ (D), Na₂Mn₃O₇ (E) and CeO₂ (F) under the 30th minute for each temperature. DFT modeling of oxygen vacancies formation (G), oxygen adspecies stability (H) and adsorption of NO and NO₂ (I) on the (1-10) facet of Na₂Mn₃O₇, along with proposed reaction mechanisms of soot combustion on the Ce-Na₂Mn₃O₇ catalyst (J). The optimized structure of the (1-10) termination (Ga₁), and formation of oxygen O_{2c} and O_{3c} vacancies of different configurations (Gb₁-f₁). The geometries of the bridging bidentate dioxygen (Ha₂) and monoatomic oxygen (Hb₂), bridging O and O₂ species (Hc₂), bridging monodentate O₂ (Hd₂), and monodentate (He₂) dioxygen adspecies. Adsorption of NO (Ia₃, Ib₃, Ic₃) and NO₂ (Id₃, Ie₃) on the (1-10) facet of the Na₂Mn₃O₇ catalyst, and the 2D diagram of their thermodynamic stability on the surface as a function of temperature and pressure (Gg₁, Hf₂, If₃), delineating the conditions of the bare (yellow area) and defected (orange to brown) surface state of the catalyst (Gg₁). The red/pink spheres, green spheres and orange cubes represent O_{3c}, O_{2c} atoms, Mn atoms and oxygen vacancies, respectively, whereas the pale and dark blue indicate O and N atoms of the nitric oxide molecule.

(1415 cm^{-1}), and bridging bidentate nitrate (1598 cm^{-1}), appear, and their intensities are increasing with the temperature. The nitrate and nitrite adspecies are also formed on the surface of the 1% Ce- $\text{Na}_2\text{Mn}_3\text{O}_7$ catalyst, even if O_2 is absent (Fig. 6B) [13,86–89]. For comparison purposes, the comparative spectra under 400 °C for Conditions 1 and 2 were also obtained (Fig. 6C), further indicating that the intensities of their IR bands are weaker than those observed in the presence of oxygen.

To explore the evolution of the adsorbed NO_x species, the in-situ isothermal DRIFTS of NO adsorption on 1% Ce- $\text{Na}_2\text{Mn}_3\text{O}_7$ as a function of time were carried out (Fig. S12), and these measurement results under the 30th minute for each temperature are also summarized in the Fig. 6D. For the 1% Ce- $\text{Na}_2\text{Mn}_3\text{O}_7$ catalyst, the accumulation of NO_x adspecies, monodentate nitrite (1365 cm^{-1}), monodentate nitrate (1444 cm^{-1}), nitro compound (1409 cm^{-1}), bridging NO_3 or gaseous or weakly adsorbed NO_2 (1625 cm^{-1}) and nitrosyls (1786 cm^{-1}), can be observed at room temperature, with the increasing time (Fig. S12A) [90, 91]. However, the NO_x species are significantly transformed when the reaction temperature increases to 100 °C (Fig. 6D). Within 10 min, weaker vibration bands at 1212 cm^{-1} (chelating and bridging nitrates) and 1267 cm^{-1} (monodentate nitrate) along with stronger bands at 1376 cm^{-1} (ionic nitrate) and 1405 cm^{-1} (nitro compound) can be distinguished. The intensity of the band 1212–1267 cm^{-1} decreases with the elapsing time, while the intensity of the bands at 1376–1405 cm^{-1} increases in the intensity (Fig. S12B). The monodentate nitrate (1264 cm^{-1}), monodentate nitrite (1332 cm^{-1}) and bidentate nitrate (1575 cm^{-1}) are formed at 200 °C within 5 min, while the major ionic nitrates (1380 cm^{-1}) species are produced with a delay (Fig. S12C). Thus, NO_x adspecies existing on the catalyst surface at 300 °C and 400 °C are the ionic nitrate and nitro compounds, indicating that they may participate in the soot oxidation at high temperature, as shown in Fig. 6D. To much deeply investigate the NO adsorption on the different catalysts, the isothermal in-situ DRIFTS of NO adsorption on the $\text{Na}_2\text{Mn}_3\text{O}_7$ and CeO_2 catalysts were also studied (Figs. 6E, 6F and Figs. S13, S14). As shown in Fig. 6E and S13, the NO_x adspecies on the $\text{Na}_2\text{Mn}_3\text{O}_7$ are different from that observed on the 1% Ce- $\text{Na}_2\text{Mn}_3\text{O}_7$ catalyst at room temperature, which indicates that the doping by Ce has modified the properties of $\text{Na}_2\text{Mn}_3\text{O}_7$, and might promote more suitable adsorption sites for activation of reaction gases. However, the NO_x adspecies on $\text{Na}_2\text{Mn}_3\text{O}_7$ are similar with that of 1% Ce- $\text{Na}_2\text{Mn}_3\text{O}_7$ catalyst when temperatures are higher than 300 °C, indicating that the activated pathways of NO on $\text{Na}_2\text{Mn}_3\text{O}_7$ and Ce- $\text{Na}_2\text{Mn}_3\text{O}_7$ are similar at high temperature. For pure CeO_2 , as shown in Fig. 6F and S14, the peaks of NO_x adspecies are completely different from that of 1% Ce- $\text{Na}_2\text{Mn}_3\text{O}_7$ catalyst. Meantime, compared with 1% Ce- $\text{Na}_2\text{Mn}_3\text{O}_7$ catalyst, the intensities of the IR bands are also weaker. This observation suggests that the CeO_2 exhibited weak adsorption capacity for NO_x species. In addition, to verify the NO_x adsorption on the catalysts, the inert SiO_2 was also studied by isothermal in-situ DRIFTS under the same reaction conditions (Fig. S12F). No NO_x adsorption was detected at 30 °C, which confirms that all observed spectral features are exclusively associated with the interaction of NO and O_2 with the Ce- $\text{Na}_2\text{Mn}_3\text{O}_7$ catalysts. The results of in-situ DRIFT illustrate that the adsorbed nitrates/nitrites are acting as the intermediate reactive species in the process of soot combustion, and the NO is readily transformed into NO_2 by the ROS and the loosely bound O_{2c} species present on the surface of the catalyst.

Since the XAS data revealed that the redox properties of the Ce- $\text{Na}_2\text{Mn}_3\text{O}_7$ catalysts are essentially associated with the Mn cations, and nitrates/nitrites are only barely formed on CeO_2 (Fig. 6F) we used the initially the parent $\text{Na}_2\text{Mn}_3\text{O}_7$ catalyst as a representative working model. Analysis of the TEM images (Fig. 1 and Fig. S3) indicated that the $\text{Na}_2\text{Mn}_3\text{O}_7$ plates exhibit predominantly the basal (1–10) plane. The optimized geometry of this facet is shown in Fig. 6Ga. Two types of labile surface oxygen anions, softly bound O_{2c}^{2-} species of the 2-fold coordination (−0.63 eV) and slightly more strongly held O_{3c}^{2-} anions of trigonal coordination (−0.86 eV), may be distinguished. In Fig. 6Gb1–d1 two surface oxygen vacancies produced upon extraction of O_2 are shown in

three different topographic arrangements. The corresponding energies of their formation are in the range of 0.59–0.64 eV. Generation of the third vacancy upon release of O_{3c} is only slightly more demanding, and requires the energy of 0.7–0.73 eV in total (Fig. 6Ge₁, f₁). The thermodynamic 2D diagram shows the p , T conditions of the oxygen vacancy formation (Fig. 6Gg₁). It indicates clearly that the $\text{Na}_2\text{Mn}_3\text{O}_7$ catalyst can easily deliver active surface oxygen species already at quite low temperatures ($T > 200$ °C), providing the molecular rational for the exceptional soot oxidation activity, and the observed changes in the Mn-AOS values during the soot oxidation (see Fig. 4B).

Interaction of oxygen with the $\text{Na}_2\text{Mn}_3\text{O}_7$ catalysts leads to formation of several types of di- and monoatomic oxygen adspecies, the most stable forms are shown in Fig. 6H. The bridging bidentate diatomic (Fig. 6Ha₂) and the dissociated oxygen pair (Fig. 6Hb₂) adsorbed on the (1–10) surface are the most tightly attached ($E_{\text{ads}} = -1.08$ eV and to −0.74 eV, respectively). The stabilization energies of the bridging monoatomic (Fig. 6Hc₂), and the bridging monodentate O_2 (Fig. 6Hd₂) are equal to −0.69 eV and −0.64 eV, respectively. The weakest bound oxygen species ($E_{\text{ads}} = -0.48$ eV) correspond to a monodentate dioxygen attached to single Mn cation, shown in Fig. 6He₂. The different energetics of the oxygen adspecies is reflected in the 2D diagram (Fig. 6Hf₂), which maps their surface stabilities at different temperatures and O_2 pressures. The monodentate dioxygen adspecies are destroyed at $T < 200$ °C (see peak α in Fig. 3B), whereas the bridging bidentate dioxygen adducts are stable until ~550 °C at the reference partial pressure around 10^{-2} (soot oxidation conditions) and below 500 °C for p/p_0 around $10^{-3}/10^{-4}$ (TPD conditions).

For the oxygen partial pressure variation during the TPD experiments, analysis of the 2D diagrams shown in Fig. 6Gg₁ and 6Hf₂ allow for molecular interpretation of the α , β and γ peaks observed in O_2 -TPD (Fig. 3B). The α peak can be then associated with the release of the adsorbed monodentate $\text{O}_{2(\text{ads})}$ surface species. The most intensive complex β peak corresponds to the bridging di- and monoatomic oxygen adspecies, and release of the surface O_{2c}^{2-} and O_{3c}^{2-} oxygen anions in various configurations, explaining well the appearance of several sub-maxima in the broad β peak observed in the O_2 -TPD (see Fig. 3B). The high temperature γ peak results from reduction involving the bulk oxygen anions. The drop in the AOS values of manganese observed in operando XAS (Fig. 4B) can be then associated with the release of the O_{2c}^{2-} and O_{3c}^{2-} species, leaving oxygen multiple vacancies of various configurations. As a result, we may propose that O_{2c}^{2-} and O_{3c}^{2-} anions along with the labile monodentate oxygen adspecies are primarily responsible for the observed exceptionally low ignition temperature of the soot oxidation over the $\text{Na}_2\text{Mn}_3\text{O}_7$ based catalysts.

Recognizing strong positive effect of NO_2 on the soot combustion efficiency, we modeled interaction of NO and NO_2 , as well as the nitrates with the catalyst surface. The three types of the examined NO binding modes with the surface are shown in Fig. 6Ia₃–c₃, and their adsorption energies are equal to −0.99, −0.7 and −0.69 eV, respectively. Attachment of a NO_2 molecule is more efficient, with the energy of −1.37 eV for nitrito (Fig. 6Id₃) and −1.17 eV for nitro adspecies (Fig. 6Ie₃). The thermodynamic stabilities of the NO and NO_2 surface adducts are shown in the 2D diagram (Fig. 6If₃), where additionally the stability of the most persistent monatomic oxygen adspecies is also delineated (dotted green line on the right). In Fig. 6If₃, the lines of d_3' , e_3' and c_3' stand for NO_2 release that is produced by an intrafacial oxidation of the corresponding NO adspecies d_3 , e_3 and c_3 in Fig. 1, by the adjacent surface O_{2c}^{2-} anion ($\text{NO}_{\text{ads}} + \text{O}_{2c}^{2-} \rightarrow \text{NO}_{2(\text{g})} + \text{V}_\text{O}$), leaving an oxygen vacancy behind. This finding supports nicely formation of surface nitrites/nitrates in the absence of dioxygen observed in the in situ DRIFT experiments (see above). The results reveal that within the stability regions of the adsorbed NO and NO_2 the monoatomic oxygen adspecies are always present. This process occurs in the range of the soot oxidation temperatures, in accordance with the operando XAS results.

In addition, apart from NO and NO_2 adspecies, surface nitrates revealed by IR measurements (Fig. 6A–E and Figs. S12, S13) may also be

involved in the soot combustion. The structures of the bidentate and monodentate nitrates are shown in Fig. S15A–C. The binding energies for a bidentate adduct A is equal to -2.19 eV, for B is -2.09 eV, whereas in the case of a monodentate adduct C it changes to -1.55 eV. The 2D diagram (Fig. S15D) shows the thermodynamic stability of the surface nitrates. Transformation of nitrates into nitrites, $\text{NO}_3^- + \text{NO} \rightarrow \text{NO}_2^- + \text{NO}_2$, both observed by IR, is another important source of NO_2 generation. For the NO pressure of p_{NO}/p_0 of 10^{-2} this reaction, was found to be thermodynamically favored in the whole temperature region for the monodentate nitrates ($\Delta G < -2$ eV), but is only barely feasible above ~ 100 °C for the most stable bridging nitrates (ΔG around -0.2 eV).

To evaluate the influence of Ce incorporation into the $\text{Na}_2\text{Mn}_3\text{O}_7$ matrix analogous DFT modeling was performed for oxygen vacancy formation (Fig. S16), as well as for various oxygen adspecies and surface nitrate stabilities (Fig. S17 and S18). The surface energy of the exposed (1–10) plane of $\text{Na}_2\text{Mn}_3\text{O}_7$ is dropped from 0.35 kJ/m² to 0.30 J/m² upon doping, indicating an appreciable stabilizing effect of Ce incorporation. Comparison of the energies of the oxygen vacancy formation shows that release of the surface O_{2c} anions is easier for the undoped catalyst (0.63 eV) than for the Ce-doped $\text{Na}_2\text{Mn}_3\text{O}_7$ (0.71 eV). However, for both types of the surface O_{3c} anions an opposite effect was found, and the vacancy formation energies decrease from 0.83 eV to 0.76 eV for type I O_{3c} , and from 1.50 – 1.30 eV for type II. (Fig. S16B, C), accounting well for the observed shift of the reduction onset in the H_2 -TPR profiles upon ceria doping (Fig. 3 A).

Among all the examined surface oxygen adspecies for the bare $\text{Na}_2\text{Mn}_3\text{O}_7$ sample only a monodentate and bidentate adducts are stable in the vicinity of the Ce cation (Fig. S17). The monodentate species A are more stable (-1.02 eV) in comparison to the corresponding adduct in the bare catalyst (-0.69 eV, structure e_2), whereas the bidentate one (B) is less stable (-0.51 eV vs -0.96 eV, structure a_2). The oxygen molecules attached directly to the Ce atom turn to be unstable. These results corroborate the displacement of the maxima of the β -band toward lower temperatures in the O_2 -TPD desorption profiles (Fig. 3B).

Similar effects of Ce-doping was observed in the case of nitrate adspecies (Fig. S18A, B). The stable forms correspond to dissociative (A) and associative (B) adsorption, with the energies of -1.78 and -0.70 eV, respectively. These values are significantly lowered with respect to the corresponding adspecies produced on the bare $\text{Na}_2\text{Mn}_3\text{O}_7$ (-2.09 and -1.55 eV, respectively). Inspection of the corresponding 2D diagram of the thermodynamic stability (Fig. S18C), indicates that the species A can release NO_2 above ~ 200 °C, which is beneficial for soot combustion, explaining also evolution of NO_2 in the NO oxidation experiments, enhanced in the presence of Ce (Fig. 3E).

Based on the above experimental results, the possible reaction mechanisms of soot combustion on the Ce- $\text{Na}_2\text{Mn}_3\text{O}_7$ catalyst were proposed, and shown in the Fig. 6 J. Due to the instability of NO adducts above 200 °C, the beneficial NO_2 (along with surface nitrates) may be effectively produced by the suprafacial Eley-Rideal mechanism in the temperature window of the soot combustion, since a possible Langmuir–Hinshelwood pathway is ceasing around 150 – 200 °C. Notably, since the NO_2 molecules produced either via the suprafacial or intrafacial oxidation of NO are readily desorbed from the catalyst surface above 150 – 200 °C, there is a permanent thermodynamic driving force for gaseous NO_2 supply in a broad range of the soot oxidation conditions, which is advantageous for promoting the soot combustion. More importantly, two kinds of Ce species, i.e. single atom Ce and CeO_2 NPs, play important roles in soot combustion. The doping of single Ce atoms will contribute to the formation of the oxygen vacancies and enhance the number of adsorption sites for reaction gases. The interfacial interactions between of CeO_2 NPs and $\text{Na}_2\text{Mn}_3\text{O}_7$ are also beneficial for the activation of oxygen species. Additionally, the high porosity of the Ce- $\text{Na}_2\text{Mn}_3\text{O}_7$ catalysts favors the NO_2 permeation, improving its intimate contact with the soot particles.

4. Conclusions

In summary, a new type of Ce-doped layer $\text{Na}_2\text{Mn}_3\text{O}_7$ catalysts (Ce- $\text{Na}_2\text{Mn}_3\text{O}_7$) were synthesized via a simple method and they exhibited excellent catalytic performance for soot combustion at low temperature. The results of in-situ DRIFTS, NO-TPO, TPR and operando XAS illustrated that the reaction mechanisms were related to facile formation of oxygen vacancies, reactive surface oxygen species and efficient NO_2 production. The above properties were controlled by the Mn redox and also were indirectly influenced by the Ce-doping. As identified by the corroborative DFT/FPT calculations, the low coordinated O_{2c}^- and O_{3c}^- anions located on the (1–10) surface along with the adsorbed reactive oxygen species play a key role in the soot combustion and the NO oxidation processes. Based on the advantages of easy synthesis, low cost, high activity and stability, the Ce- $\text{Na}_2\text{Mn}_3\text{O}_7$ catalysts are promising materials for practical applications in the catalytic oxidation of diesel soot particles. More importantly, the developed catalysts could be applied in various heterogeneous oxidation reactions. This work may be useful for rational design and facile preparation of other highly efficient oxidation catalysts through doping alien cations into the parent $\text{Na}_2\text{Mn}_3\text{O}_7$ layers.

CRediT authorship contribution statement

Di Yu: Data curation, Formal analysis, Investigation, Methodology, Writing – original draft. **Xuehua Yu:** Data curation, Formal analysis, Investigation, Methodology, Writing – review & editing, Funding acquisition, Project administration. **Chunlei Zhang:** Data curation, Formal analysis, Investigation, Methodology. **Lanyi Wang:** Data curation, Formal analysis, Visualization. **Xiaoqiang Fan:** Data curation, Investigation, Formal analysis. **Zhen Zhao:** Conceptualization, Funding acquisition, Project administration, Resources, Supervision, Validation, Writing – review & editing. **Yuechang Wei:** Investigation, Formal analysis, Software, Visualization. **Jian Liu:** Investigation, Formal analysis, Software, Visualization. **Joanna Gryboś:** Data curation, Formal analysis, Investigation, Software. **Bartosz Leszczyński:** Formal analysis, Visualization, Software. **Anna Wach:** Data curation, Formal analysis, Investigation, Visualization. **Dominik Wierzbicki:** Formal Analysis, Investigation, Software. **Andrzej Kotarba:** Formal analysis, Investigation, Software, Visualization. **Zbigniew Sojka:** Formal analysis, Software, Visualization, Funding acquisition, Writing – review & editing.

Declaration of Competing Interest

The authors declare that they have no known competing financial interests or personal relationships that could have appeared to influence the work reported in this paper.

Data Availability

The authors do not have permission to share data.

Acknowledgements

We acknowledge the financial support from National Key R&D Program of China (2022YFB3506200, 2022YFB3504100); National Natural Science Foundation of China (22072095, U1908204); Liaoning Provincial Central Government Guides Local Science and Technology Development Funds (2022JH6/100100052); Excellent Youth Science Foundation of Liaoning Province (2022-YQ-20); University Joint Education Project for China-Central and Eastern European Countries (2021097); Major/Key Project of Graduate Education and Teaching Reform of Shenyang Normal University (YJSJG120210008/YJSJG220210022); Shenyang Science and Technology Planning Project (22-322-3-28); University level innovation team of Shenyang Normal University and the NCBR Program MOST (WPC/4/PNOX/2018) of

Poland, and The National Centre for Research and Development, Poland, grant PNOX no. WPC1/PNOX/2019 (MOST program). We thank the Paul Scherrer Institute, Villigen, Switzerland for the synchrotron beamline SuperXAS-X10DA of SLS, and Dr Piotr Legutko and Grigory Smolentsev for their assistance during the measurements.

Appendix A. Supporting information

Supplementary data associated with this article can be found in the online version at [doi:10.1016/j.apcatb.2023.123022](https://doi.org/10.1016/j.apcatb.2023.123022).

References

- [1] R. Niessner, The many faces of soot: characterization of soot nanoparticles produced by engines, *Angew. Chem. Int. Ed.* 53 (2014) 12366–12379.
- [2] B. Frank, M.E. Schuster, R. Schlögl, D.S. Su, Emission of highly activated soot particulate-the other side of the coin with modern diesel engines, *Angew. Chem. Int. Ed.* 52 (2013) 2673–2677.
- [3] H. Yamada, S. Inomata, H. Tanimoto, Mechanisms of increased particle and VOC emissions during DPF active regeneration and practical emissions considering regeneration, *Environ. Sci. Technol.* 51 (2017) 2914–2923.
- [4] X. Mei, X. Zhu, Y. Zhang, Z. Zhang, Z. Zhong, Y. Xin, J. Zhang, Decreasing the catalytic ignition temperature of diesel soot using electrified conductive oxide catalysts, *Nat. Catal.* 4 (2021) 1002–1011.
- [5] Y.C. Wei, P. Zhang, J. Xiong, Q. Yu, Q.Q. Wu, Z. Zhao, J. Liu, SO₂-tolerant catalytic removal of soot particles over 3D ordered macroporous Al₂O₃-supported binary Pt-Co oxide catalysts, *Environ. Sci. Technol.* 54 (2020) 6947–6956.
- [6] X.H. Yu, Y. Ren, D. Yu, M.Z. Chen, L.Y. Wang, R.D. Wang, X.Q. Fan, Z. Zhao, K. Cheng, Y.S. Chen, J. Grybos, A. Kotarba, Z. Sojka, Y.C. Wei, J. Liu, Hierarchical porous K-OMS-2/3DOM-m TiO₂/SiO₂ catalysts for soot combustion: Easy preparation, high catalytic activity, and resistance to H₂O and SO₂, *ACS Catal.* 11 (2021) 5554–5571.
- [7] M. Wang, Y. Zhang, Y.B. Yu, W.P. Shan, Synergistic effects of multicomponents produce outstanding soot oxidation activity in a Cs/Co/MnO_x catalyst, *Environ. Sci. Technol.* 55 (2021) 240–248.
- [8] X. Feng, J. Xu, X. Xu, S. Zhang, X. Wang, Unraveling the principles of lattice disorder degree of Bi₂B₂O₇ (B = Sn, Ti, Zr) compounds on activating gas phase O₂ for soot combustion, *ACS Catal.* 11 (2021) 12112–12122.
- [9] L.J. He, Y. Zhang, Y.C. Zang, C.X. Liu, W.C. Wang, R. Han, N. Ji, S.T. Zhang, Q. L. Liu, Promotion of A-site Ag-doped perovskites for the catalytic oxidation of soot: synergistic catalytic effect of dual active sites, *ACS Catal.* 11 (2021) 14224–14236.
- [10] G. Yu, J. Wang, H.M. Ma, X.J. Liu, S.J. Qin, Z.G. Yang, G.L. Zhang, Y.T. Li, L.Y. Zhu, Exploring abundantly synergistic effects of K-Cu supported paper catalysts using TiO₂-ZrO₂ mesoporous fibers as matrix towards soot efficient oxidation, *Chem. Eng. J.* 417 (2021), 128111.
- [11] Q.L. Shi, T.Z. Liu, Q. Li, Y. Xin, X.X. Lu, W.X. Tang, Z.L. Zhang, P.X. Gao, J. A. Anderson, Multiple strategies to decrease ignition temperature for soot combustion on ultrathin MnO_{2-x} nanosheet array, *Appl. Catal. B: Environ.* 246 (2019) 312–321.
- [12] B. Sellers-Antón, E. Bailón-García, A. Cardenas-Arenas, A. Davó-Quinonero, D. Lozano-Castelló, A. Bueno-López, Enhancement of the generation and transfer of active oxygen in Ni/CeO₂ catalysts for soot combustion by controlling the Ni-ceria contact and the three-dimensional structure, *Environ. Sci. Technol.* 54 (2020) 2439–2447.
- [13] M.J. Zhao, J.L. Deng, J. Liu, Y.H. Li, J.X. Liu, Z.C. Duan, J. Xiong, Z. Zhao, Y. C. Wei, W.Y. Song, Y.Q. Sun, Roles of surface-active oxygen species on 3DOM cobalt-based spinel catalysts M₂Co_{3-x}O₄ (M = Zn and Ni) for NO_x-assisted soot oxidation, *ACS Catal.* 9 (2019) 7548–7567.
- [14] Y. Tsai, N.N. Huy, J. Lee, Y. Lin, K.A. Lin, Catalytic soot oxidation using hierarchical cobalt oxide microspheres with various nanostructures: insights into relationships of morphology, property and reactivity, *Chem. Eng. J.* 395 (2020), 124939.
- [15] P. Zhang, X. Mei, X. Zhao, J. Xiong, Y. Li, Z. Zhao, Y. Wei, Boosting catalytic purification of soot particles over double perovskite-type La_{2-x}K_xNiCoO₆ catalysts with an ordered macroporous structure, *Environ. Sci. Technol.* 55 (2021) 11245–11254.
- [16] Q. Wu, M. Jing, Y. Wei, Z. Zhao, X. Zhang, J. Xiong, J. Liu, W. Song, J. Li, High-efficient catalysts of core-shell structured Pt@transition metal oxides (TMOs) supported on 3DOM-Al₂O₃ for soot oxidation: the effect of strong Pt-TMO interaction, *Appl. Catal. B: Environ.* 244 (2019) 628–640.
- [17] J. Xiong, Q. Wu, X. Mei, J. Liu, Y. Wei, Z. Zhao, D. Wu, J. Li, Fabrication of spinel-type Pd₃Co_{3-x}O₄ binary active sites on 3D ordered meso-macroporous Ce-Zr-O₂ with enhanced activity for catalytic soot oxidation, *ACS Catal.* 8 (2018) 7915–7930.
- [18] Y. Wei, Y. Zhang, P. Zhang, J. Xiong, X. Mei, Q. Yu, Z. Zhao, J. Liu, Boosting the removal of diesel soot particles by the optimal exposed crystal facet of CeO₂ in Au/CeO₂ catalysts, *Environ. Sci. Technol.* 54 (2020) 2002–2011.
- [19] H.L. Wang, B.F. Jin, H.B. Wang, N.N. Ma, W. Liu, D. Weng, X.D. Wu, S. Liu, Study of Ag promoted Fe₂O₃@CeO₂ as superior soot oxidation catalysts: the role of Fe₂O₃ crystal plane and tandem oxygen delivery, *Appl. Catal. B: Environ.* 237 (2018) 251–262.
- [20] A. Serve, A. Boreave, B. Cartoixa, K. Pajot, P. Vernoux, Synergy between Ag nanoparticles and yttria-stabilized zirconia for soot oxidation, *Appl. Catal. B: Environ.* 242 (2019) 140–149.
- [21] Y.C. Wei, J. Liu, Z. Zhao, Y.S. Chen, C.M. Xu, A.J. Duan, G.Y. Jiang, H. He, Highly active catalysts of gold nanoparticles supported on three-dimensionally ordered macroporous LaFeO₃ for soot oxidation, *Angew. Chem. Int. Ed.* 50 (2011) 2326–2329.
- [22] J.H. Lee, S.H. Lee, J.W. Choung, C.H. Kim, K.Y. Lee, Ag-incorporated macroporous CeO₂ catalysts for soot oxidation: Effects of Ag amount on the generation of active oxygen species, *Appl. Catal. B: Environ.* 246 (2019) 356–366.
- [23] Y.F. Shen, R.P. Zerger, R.N. Deguzman, S.L. Suib, L. McCurdy, D.I. Potter, C. L. O'young, Manganese oxide octahedral molecular sieves: preparation, characterization, and applications, *Science* 260 (1993) 511–515.
- [24] B. Dutta, R. Clarke, S. Raman, T.D. Shaffer, L. Achola, P. Nandi, S.L. Suib, Lithium promoted mesoporous manganese oxide catalyzed oxidation of allyl ethers, *Nat. Commun.* 10 (2019) 655.
- [25] C. Lin, J.L. Li, X.P. Li, S. Yang, W. Luo, Y.J. Zhang, S.H. Kim, D.H. Kim, S. S. Shinde, Y.F. Li, Z.P. Liu, Z. Jiang, J.H. Lee, In-situ reconstructed Ru atom array on α-MnO₂ with enhanced performance for acidic water oxidation, *Nat. Catal.* 4 (2021) 1012–1023.
- [26] B. Lin, X. Zhu, L. Fang, X. Liu, S. Li, T. Zhai, L. Xue, Q. Guo, J. Xu, H. Xia, Birnessite nanosheet arrays with high K content as a high-capacity and ultrastable cathode for K-ion batteries, *Adv. Mater.* 31 (2019), 1900060.
- [27] H. Zhao, H. Li, Z. Pan, F. Feng, Y. Gu, J. Du, Y. Zhao, Design of CeMnCu ternary mixed oxides as soot combustion catalysts based on optimized Ce/Mn and Mn/Cu ratios in binary mixed oxides, *Appl. Catal. B: Environ.* 268 (2020), 118422.
- [28] R.J. Yang, Y.Y. Fan, R.Q. Ye, Y.X. Tang, X.H. Cao, Z.Y. Yin, Z.Y. Zeng, MnO₂-based materials for environmental applications, *Adv. Mater.* 33 (2021), 2004862.
- [29] J. Grybos, M. Fedyna, P. Legutko, B. Leszczyński, J. Janas, A. Wach, J. Szelachetko, X. Yu, A. Kotarba, Z. Zhao, Z. Sojka, Mechanistic insights into oxygen dynamics in soot combustion over cryptomelane catalysts in tight and loose contact modes via ¹⁸O/¹⁶O isotopic variable composition measurements—a hot ring model of the catalytic operation, *ACS Catal.* 11 (2021) 9530–9546.
- [30] T.Z. Liu, Q. Li, Y. Xin, Z.L. Zhang, X.F. Tang, L.R. Zheng, P.X. Gao, Quasi free K cations confined in hollandite-type tunnels for catalytic solid (catalyst)-solid (reactant) oxidation reactions, *Appl. Catal. B: Environ.* 232 (2018) 108–116.
- [31] M.E. Becerra, N.P. Arias, O.H. Giraldo, F.E. López Suárez, M.J. Illán Gómez, A. Bueno, López, Soot combustion manganese catalysts prepared by thermal decomposition of KMnO₄, *Appl. Catal. B: Environ.* 102 (2011) 260–266.
- [32] R. Kimura, J. Wakabayashi, S.P. Elangovan, M. Ogura, T. Okubo, Nepheline from K₂CO₃/nanosized sodalite as a prospective candidate for diesel soot combustion, *J. Am. Chem. Soc.* 130 (2008) 12844–12845.
- [33] J.P. Parant, R. Olazcuaga, M. Devalette, C. Fouassier, P. Hagenmuller, Sur quelques nouvelles phases de formule Na_xMnO₂ (x<1), *J. Solid State Chem.* 3 (1971) 1–11.
- [34] S. Boyd, K. Ganesan, W.Y. Tsai, T. Wu, S. Saeed, D.E. Jiang, N. Balke, A.C.T. van Duin, V. Augustyn, Effects of interlayer confinement and hydration on capacitive charge storage in birnessite, *Nat. Mater.* 20 (2021) 1689–1694.
- [35] A. Tsuchimoto, X.M. Shi, K. Kawai, B.M. de Boisse, J. Kikkawa, D. Asakura, M. Okubo, A. Yamada, Nonpolarizing oxygen-redox capacity without O-O dimerization in Na₂Mn₃O₇, *Nat. Commun.* 12 (2021) 631.
- [36] Q.N. Liu, Z. Hu, W.J. Li, C. Zou, H.L. Jin, S. Wang, S.L. Chou, S.X. Dou, Sodium transition metal oxides: the preferred cathode choice for future sodium-ion batteries, *Energy Environ. Sci.* 14 (2021) 158–179.
- [37] B. Song, M. Tang, E. Hu, O.J. Borkiewicz, K.M. Właderek, Y. Zhang, N.D. Phillip, X. Liu, Z. Shadike, C. Li, L. Song, Y. Hu, M. Chi, G.M. Veith, X. Yang, J. Liu, J. Nanda, K. Page, A. Huq, Understanding the low-voltage hysteresis of anionic redox in Na₂Mn₃O₇, *Chem. Mater.* 31 (2019) 3756–3765.
- [38] D.A. Kitchaev, J. Vinckeviciute, A.V.D. Ven, Delocalized metal-oxygen π- redox is the origin of anomalous nonhysteretic capacity in Li-ion and Na-ion cathode materials, *J. Am. Chem. Soc.* 143 (2021) 1908–1916.
- [39] E. Adamczyk, V. Pralong, Na₂Mn₃O₇: a suitable electrode material for Na-ion batteries? *Chem. Mater.* 29 (2017) 4645–4648.
- [40] L. Nie, D.H. Mei, H.F. Xiong, B. Peng, Z.B. Ren, X.I.P. Hernandez, A. DeLaRiva, M. Wang, M.H. Engelhard, L. Kovarik, A.K. Datye, Y. Wang, Activation of surface lattice oxygen in single-atom Pt/CeO₂ for low-temperature CO oxidation, *Science* 358 (2017) 1419–1423.
- [41] N. Daelman, M. Capdevila-Cortada, N. López, Dynamic charge and oxidation state of Pt/CeO₂ single-atom catalysts, *Nat. Mater.* 18 (2019) 1215–1221.
- [42] C.T. Campbell, C.H.F. Peden, Oxygen vacancies and catalysis on ceria surfaces, *Science* 309 (2005) 713–714.
- [43] V. Muravev, G. Spezzati, Y.Q. Su, A. Parastaev, F.K. Chiang, A. Longo, C. Escudero, N. Kosinov, E.J.M. Hensen, Interface dynamics of Pd-CeO₂ single-atom catalysts during CO oxidation, *Nat. Catal.* 4 (2021) 469–478.
- [44] T. Montini, M. Melchionna, M. Monai, P. Fornasiero, Fundamentals and catalytic applications of CeO₂-based materials, *Chem. Rev.* 116 (2016) 5987–6041.
- [45] M. Machida, Y. Murata, K. Kishikawa, D. Zhang, K. Ikeue, On the reasons for high activity of CeO₂ catalyst for soot oxidation, *Chem. Mater.* 20 (2008) 4489–4494.
- [46] E. Aneggi, D. Wiat, C. De Leitenburg, J. Llorca, A. Trovarelli, A. Shape-dependent activity of ceria in soot combustion, *ACS Catal.* 4 (2014) 172–181.
- [47] P. Legutko, P. Stelmachowski, M. Trebala, Z. Sojka, A. Kotarba, A. Role of electronic factor in soot oxidation process over tunnelled and layered potassium iron oxide catalysts, *Top. Catal.* 56 (2013) 489–492.
- [48] K. Mori, Y. Miyauchi, Y. Kuwahara, H. Yamashita, Shape effect of MnO_x-decorated CeO₂ catalyst in diesel soot oxidation, *B. Chem. Soc. Jpn.* 90 (2017) 556–564.
- [49] B. Ravel, M. Newville, Athena, artemis, hephaestus: data analysis for X-ray absorption spectroscopy using IFEFIT, *J. Synchrotron Radiat.* 12 (2005) 537–541.

- [50] S.I. Zabinsky, J.J. Rehr, A. Ankudinov, R.C. Albers, M.J. Eller, Multiple-scattering calculations of X-ray-absorption spectra, *Phys. Rev. B* 52 (1995) 2995–3009.
- [51] H. Funke, A.C. Scheinost, M. Chukalina, Wavelet analysis of extended X-ray absorption fine structure data, *Phys. Rev. B* 71 (2005), 094110.
- [52] A.V. Fedorov, R.G. Kukushkin, P.M. Yeletsky, O.A. Bulavchenko, Y.A. Chesalov, V. A. Yakovlev, Temperature-programmed reduction of model CuO, NiO and mixed CuO/NiO catalysts with hydrogen, *J. Alloy. Compd.* 844 (2020), 156135.
- [53] Z. Yuan, L. Wang, J. Wang, S. Xia, P. Chen, Z. Hou, X. Zheng, Hydrogenolysis of glycerol over homogeneously dispersed copper on solid base catalysts, *Appl. Catal. B: Environ.* 101 (2011) 431–440.
- [54] X.L. Deng, M.X. Li, J. Zhang, X.Y. Hu, J.B. Zheng, N.W. Zhang, B.H. Chen, Constructing nano-structure on silver/ceria-zirconia towards highly active and stable catalyst for soot oxidation, *Chem. Eng. J.* 313 (2017) 544–555.
- [55] L. Zhu, J. I Wang, S.P. Rong, H.Y. Wang, P.Y. Zhang, Cerium modified birnessite-type MnO₂ for gaseous formaldehyde oxidation at low temperature, *Appl. Catal. B: Environ.* 211 (2017) 212–221.
- [56] L. Chen, G. Liu, N. Feng, J. Yu, J. Meng, F. Fang, P. Zhao, L. Wang, H. Wan, G. Guan, Effect of calcination temperature on structural properties and catalytic soot combustion activity of MnO_x/wire-mesh monoliths, *Appl. Surf. Sci.* 467–468 (2019) 1088–1103.
- [57] H. Chang, X. Chen, J. Li, L. Ma, C. Wang, C. Liu, J.W. Schwank, J. Hao, Improvement of activity and SO₂ tolerance of Sn-modified MnO_x-CeO₂ catalysts for NH₃-SCR at low temperatures, *Environ. Sci. Technol.* 47 (2013) 5294–5301.
- [58] X. Lin, S. Li, H. He, Z. Wu, J. Wu, L. Chen, D. Ye, M. Fu, Evolution of oxygen vacancies in MnO_x-CeO₂ mixed oxides for soot oxidation, *Appl. Catal. B: Environ.* 22 (2018) 91–102.
- [59] H. Hui, X.T. Lin, S.J. Li, Z. Wu, J.H. Gao, J.L. Wu, W. William, D.Q. Ye, M.L. Fu, The key surface species and oxygen vacancies in MnO_x(0.4)-CeO₂ toward repeated soot oxidation, *Appl. Catal. B: Environ.* 223 (2018) 134–142.
- [60] J.C. Li, X. Qin, F. Xiao, C. Liang, M. Xu, Y. Meng, E. Sarnello, L. Fang, T. Li, S. Ding, Z. Lyu, S. Zhu, X. Pan, P. Hou, C. Liu, Y. Lin, M. Shao, Highly dispersive cerium atoms on carbon nanowires as oxygen reduction reaction electrocatalysts for Zn-Air batteries, *Nano Lett.* 21 (2021) 4508–4515.
- [61] Y.F. Zheng, Q. Liu, C. Shan, Y. Su, K. Fu, S. Lu, R. Han, C. Song, N. Ji, D. Ma, Defective ultrafine MnO_x nanoparticles confined within a carbon matrix for low-temperature oxidation of volatile organic compounds, *Environ. Sci. Technol.* 55 (2021) 5403–5411.
- [62] T.Y. Luo, S. Liu, M. Li, W. Liu, X. Wu, S. Liu, Ozone-assisted diesel soot combustion over Mn₂O₃ catalysts: A tandem work of different reactive phases, *J. Catal.* 408 (2022) 56–63.
- [63] G. Nagaraju, Y.H. Ko, S.M. Cha, S.H. Im, J.S. Yu, A facile one-step approach to hierarchically assembled core-shell-like MnO₂@MnO₂ nanoarchitectures on carbon fibers: An efficient and flexible electrode material to enhance energy storage, *Nano Res.* 9 (2016) 1507–1522.
- [64] J.T. Hou, Y.Z. Li, M.Y. Mao, L. Ren, X.J. Zhao, Tremendous effect of the morphology of birnessite-type manganese oxide nanostructures on catalytic activity, *ACS Appl. Mater. Interfaces* 6 (2014) 14981–14987.
- [65] J. Xiong, Y.C. Wei, Y.L. Zhang, P. Zhang, Q. Yu, X.L. Mei, X. Liu, Z. Zhao, J. Liu, Synergetic Effect of K Sites and Pt Nanoclusters in an Ordered Hierarchical Porous Pt-KMnO₄/Ce_{0.25}Zr_{0.75}O₂ Catalyst for Boosting Soot Oxidation, *ACS Catal.* 10 (2020) 7123–7135.
- [66] Q.H. Yan, Y.S. Gao, Y.R. Li, M.A. Vasilades, S.N. Chen, C. Zhang, R.R. Gui, Q. Wang, T.Y. Zhu, A.M. Efsthathiou, Promotional effect of Ce doping in Cu₄Al₂O₇–LDO catalyst for low-T practical NH₃-SCR: Steady-state and transient kinetics studies, *Appl. Catal. B: Environ.* 255 (2019), 117749.
- [67] D. Yu, L.Y. Wang, C.L. Zhang, C. Peng, X.H. Yu, X.Q. Fan, B. Liu, K.X. Li, Z.G. Li, Y. C. Wei, J. Liu, Z. Zhao, Alkali metals and Cerium-modified La–Co-based perovskite catalysts: facile synthesis, excellent catalytic performance, and reaction mechanisms for soot combustion, *ACS Catal.* 12 (2022) 15056–15075.
- [68] M.J. Kim, E.J. Lee, E. Lee, D.H. Kim, D.W. Lee, C.H. Kim, K.Y. Lee, Ag-doped manganese oxide catalyst for gasoline particulate filters: effect of crystal phase on soot oxidation activity, *Appl. Surf. Sci.* 569 (2021), 151041.
- [69] X.H. Feng, R. Liu, X.L. Xu, Y.Y. Tong, S.J. Zhang, J.C. He, J.W. Xu, X.Z. Fang, X. Wang, Stable CuO/La₂Sn₂O₇ catalysts for soot combustion: study on the monolayer dispersion behavior of CuO over a La₂Sn₂O₇ pyrochlore support, *Chinese, J. Catal.* 42 (2021) 396–408.
- [70] B. Cui, L. Zhou, K. Li, Y. Liu, D. Wang, Y. Ye, S. Li, Holey Co-Ce oxide nanosheets as a highly efficient catalyst for diesel soot combustion, *Appl. Catal. B: Environ.* 267 (2020), 118670.
- [71] Y. Cheng, J. Liu, Z. Zhao, W.Y. Song, Y.C. Wei, Highly efficient and simultaneously catalytic removal of PM and NO_x from diesel engines with 3DOM Ce_{0.8}Mn_{0.1}Zr_{0.1}O₂ (M = Mn, Co, Ni) catalysts, *Chem. Eng. Sci.* 167 (2017) 219–228.
- [72] N. Russo, D. Fino, G. Saracco, V. Specchia, Studies on the redox properties of chromite perovskite catalysts for soot combustion, *J. Catal.* 229 (2005) 459–469.
- [73] D. Jampaiah, V.K. Velisoju, P. Venkataswamy, V.E. Coyle, A. Nafady, B.M. Reddy, S.K. Bhargava, Nanowire morphology of mono- and bidoped α-MnO₂ catalysts for remarkable enhancement in soot oxidation, *ACS Appl. Mater. Interfaces* 9 (2017) 32652–32666.
- [74] W. Ren, T. Ding, Y.X. Yang, L.L. Xing, Q.P. Cheng, D.Y. Zhao, Z.L. Zhang, Q. Li, J. Zhang, L.R. Zheng, Identifying oxygen activation/oxidation sites for efficient soot combustion over silver Catalysts interacted with nanoflower-like hydrotalcite-derived CoAlO metal oxides, *ACS Catal.* 9 (2019) 8772–8784.
- [75] M. Wang, Y. Zhang, Y.B. Yu, W.P. Shan, H. He, Cesium as a dual function promoter in Co/Ce-Sn catalyst for soot oxidation, *Appl. Catal. B: Environ.* 285 (2021), 119850.
- [76] I. Meza-Trujillo, A. Mary, P. Pietrzyk, Z. Sojka, E.M. Gaigneaux, Nature and role of Cu(II) species in doped C12A7 catalysts for soot oxidation, *Appl. Catal. B: Environ.* 316 (2022), 121604.
- [77] Z. Yang, W. Hu, N. Zhang, Y. Li, Y. Liao, Facile synthesis of ceria–zirconia solid solutions with cubic–tetragonal interfaces and their enhanced catalytic performance in diesel soot oxidation, *J. Catal.* 377 (2019) 98–109.
- [78] F. Fang, N. Feng, P. Zhao, C. Chen, X. Li, J. Meng, G. Liu, L. Chen, H. Wan, G. Guan, In situ exsolution of Co/Co₃O₄ core-shell nanoparticles on double perovskite porous nanotubular webs: A synergistically active catalyst for soot efficient oxidation, *Chem. Eng. J.* 372 (2019) 752–764.
- [79] J. Lee, M.W. Lee, M.J. Kim, J.H. Lee, E.J. Lee, C.H. Jung, J.W. Choung, C.H. Kim, K. Lee, Effects of La incorporation in catalytic activity of Ag/La-CeO₂ catalysts for soot oxidation, *J. Hazard. Mater.* 414 (2021), 125523.
- [80] Y.X. Yang, D.Y. Zhao, Z.N. Gao, Y. Tian, T. Ding, J. Zhang, Z. Jiang, X.G. Li, Interface interaction induced oxygen activation of cactus-like Co₃O₄/OMS-2 nanorod catalysts in situ grown on monolithic cordierite for diesel soot combustion, *Appl. Catal. B: Environ.* 286 (2021), 119932.
- [81] D. Yu, Y. Ren, X. Yu, X. Fan, L. Wang, R. Wang, Z. Zhao, K. Cheng, Y. Chen, Z. Sojka, A. Kotarba, Y. Wei, J. Liu, Facile synthesis of birnessite-type K₂Mn₄O₈ and cryptomelane-type K_{2-x}Mn₈O₁₆ catalysts and their excellent catalytic performance for soot combustion with high resistance to H₂O and SO₂, *Appl. Catal. B: Environ.* 285 (2021), 119779.
- [82] X.Z. Mao, S.R. Liu, W. Liu, X.D. Wu, S. Liu, A simple model catalyst study to distinguish the roles of different oxygen species in propane and soot combustion, *Appl. Catal. B: Environ.* 310 (2022), 121331.
- [83] X.H. Yu, L.Y. Wang, M.Z. Chen, X.Q. Fan, Z. Zhao, K. Cheng, Y.S. Chen, Z. Sojka, Y. C. Wei, J. Liu, Enhanced activity and sulfur resistance for soot combustion on three-dimensionally ordered macroporous-mesoporous Mn_xCe_{1-x}O₃/SiO₂ catalysts, *Appl. Catal. B: Environ.* 254 (2019) 246–259.
- [84] W. Wang, G. McCool, N. Kapur, G. Yuan, B. Shan, M. Nguyen, U. Graham, B. Davis, G. Jacobs, K. Cho, X. Hao, Mixed-phase oxide catalyst based on Mn-mullite (Sm, Gd)Mn₂O₅ for NO oxidation in diesel exhaust, *Science* 337 (2012) 832–835.
- [85] J. Hwang, R.R. Rao, L. Giordano, K. Akkijaru, X.R. Wang, E.J. Crumlin, H. Bluhm, Y. S. Horn, Regulating oxygen activity of perovskites to promote NO_x oxidation and reduction kinetics, *Nat. Catal.* 4 (2021) 663–673.
- [86] I.S. Pieta, M. García-Diéguez, C. Herrera, M.A. Larrubia, L.J. Alemany, In situ DRIFT–TRM study of simultaneous NO_x and soot removal over Pt-Ba and Pt-K NSR catalysts, *J. Catal.* 270 (2010) 256–267.
- [87] (a) I.S. Pieta, M. García-Diéguez, C. Herrera, M.A. Larrubia, L.J. Alemany, *J. Catal.* 270 (2010) 256–267; (b) Q. Shen, G. Lu, C. Du, Y. Guo, Y. Wang, Y. Guo, X. Gong, Role and reduction of NO_x in the catalytic combustion of soot over iron–ceria mixed oxide catalyst, *Chem. Eng. J.* 218 (2013) 164–172.
- [88] L. Urán, J. Gallego, W. Ruiz, E. Bailón-García, A. Bueno-López, A. Santamaría, Monitoring intermediate species formation by DRIFT during the simultaneous removal of soot and NO_x over LaAgMnO₃ catalyst, *Appl. Catal. A: Gen.* 588 (2019), 117280.
- [89] X. Yao, L. Li, W. Zou, S. Yu, J. An, H. Li, F. Yang, L. Dong, Preparation, characterization, and catalytic performance of high efficient CeO₂-MnO_x-Al₂O₃ catalysts for NO elimination, *Chin. J. Catal.* 37 (2016) 1369–1380.
- [90] C.A. Roberts, L. Savereide, D.J. Childers, T.C. Peck, J.M. Notestein, In situ FTIR spectroscopy of highly dispersed FeOx catalysts for NO reduction: Role of Na promoter, *Catal. Today* 267 (2016) 56–64.
- [91] S. Liu, X.D. Wu, D. Weng, M. Li, R. Ran, Roles of acid sites on Pt/H-ZSM5 catalyst in catalytic oxidation of diesel soot, *ACS Catal.* 5 (2015) 909–919.